Towards Implementation of Quantum Algorithms Using Electron and Nuclear Spins in Single Crystals

by

Stéphane Labruyère

A thesis
presented to the University of Waterloo
in fulfillment of the
thesis requirement for the degree of
Master of Applied Science
in
Electrical and Computer Engineering

Waterloo, Ontario, Canada, 2014

© Stéphane Labruyère 2014

Author's Declaration

I hereby declare that I am the sole author of this thesis. This is a true copy of the thesis, including any required final revisions, as accepted by my examiners.

I understand that my thesis may be made electronically available to the public.

Abstract

Quantum computing set a goal to harness the quantum laws of physics and create computers more powerful than ever imagined. Different technologies can be chosen to implement quantum bits (qubits), each with their advantages and drawbacks. The idea of combining different technologies then seems natural in order to come up with an optimal quantum computer.

In this sense, Nuclear Magnetic Resonance (NMR) and Electron Spin Resonance (ESR) seem to be the perfect marriage. Indeed, while electron spins can perform quantum gates within nanoseconds, they have to fight very fast decoherence phenomena, the nuclear spins, on the other hand, require longer electromagnetic pulses to be rotated but can be controlled longer without loss of quantum information. Using electron spins as actuators and nuclear spins as memory then appears as the optimal use of this hybrid system. Another fact accounting for this association is that the control of the system through the electron spin requires techniques very similar to the well-known NMR ones.

This work focuses on characterizing as precisely as possible the Hamiltonian of a hybrid spin system in a solid-state single crystal, especially the electron-nuclear interactions, to perform high-fidelity control in a home-built pulsed ESR spectrometer. Using this knowledge, we show that we can choose the orientation of the magnetic field with respect to our crystal to obtain optimal experimental conditions. Indeed, with a good knowledge of the Hamiltonian of the system, we want demonstrate high-fidelity quantum control.

The final aim of this work is to dynamically supply highly polarized ancilla qubits that can be used in a Quantum Error Correction (QEC) experiment by implementing heat bath algorithmic cooling using a cold electron spin bath. This is an important step towards demonstrating the viability of spin systems for building quantum computers.

Acknowledgements

Everyone's path is different when it comes to getting into research in quantum computing. I had been dreaming about it since my early science-fiction readings but even when science became something more concrete in my life, after my undergraduate studies in engineering in France, coming to Canada to work on quantum computing did not seem like the natural path to follow to many people.

Yet, one person I must acknowledge more than others actually believed my choice was not that eerie and maybe I could indeed do my bit. Prof. Jonathan Baugh, in addition of being an inspiring supervisor for his hard-work and incredible knowledge, took the risk to make me a member of his team. Jonathan knew when to push me and make me think again about a problem to finally overcome it and get closer to our common goals. Of course, my coming to IQC would not have been possible without Prof. Hamed Majedi. To me, his role at IQC is essential since designing the future quantum technologies requires the concourse of people with different backgrounds, including engineers. In addition, I must say Prof. Majedi is an amazing lecturer and it was a real pride for me, when attending his lectures, that he was my co-supervisor. I would also like to thank Prof. Raymond Laflamme. Not only did Ray co-found IQC, making all of this work -and so much more- possible, but also he has been involved in our project a lot. He always asked the right questions at the right time to make our research as efficient and useful to science as possible. Let me also thank Prof. Laflamme for agreeing to attend my MASc seminar and be on my reading committee. Prof. Miao is the other external reader for this thesis, and I thank him a lot for accepting to take this role.

Obviously, this work would not have been possible without my great teammates, Daniel (Kyundgoeck) Park and Dr Robabeh Rahimi Darabad. Daniel's extended knowledge of our pulsed ESR lab always compelled my admiration. Daniel is an outstanding experimentalist and I deeply thank him for sharing all he knew about magnetic resonance with me. Robabeh's infinite patience in looking for new crystal growth methods commanded my respect and I thank her for helping me how to use the CW spectrometer and the preparation of the experiments.

The University of Waterloo is an incredible place to work and the shared facilities it

provides are probably one of the most important reasons for its success. I would like to thank Hiruy Haile, precision machinist at the student machine shop for sharing his knowledge of machining with me. Hiruy never ran out of ideas no matter the challenges of our different designs. Dr Jalil Assoud also contributed immensely in this work. He never gave up trying to extract crystallographic structure out of the sample we gave him. For his scientific and human contributions, Jalil can undeniably be regarded as a cornerstone of this work. Let me also thank Sarah Landy, Susan Widdifield and Monica Dey, respectively ECE PhD coordinator, ECE MASc coordinator and IQC graduate studies coordinator, along with all the IQC and ECE staff. Their always quick and relevant help was a true relief anytime I had questions or enquiries in the course of my graduate program.

Eventually, I would like to thank my family and friends. A lot of international students work at IQC and it is always hard to live far from your family during several years: that gives you an idea of how much all of us love science. I thank my family for understanding my choice and being there all along, even if after all my clumsy attempts to explain what is quantum computing, they probably still have no idea what I did during these two years. I would also like to pay my tribute to all the friends I made here. They made my discovery of Canada the greatest experience in my life. My friends in France have been amazing too, doing their best to come and see me during my short stays in Europe. I am incredibly lucky to know each of them and I am always looking forward to the next moment we will share together. Last but not least, a few words for my amazing girlfriend Julie Tournet who supported me during these two years. Julie always found the right words to make me feel proud of what I was doing, even when I was desperately unsatisfied with the imperfections of my work. I can only be thankful to her for allowing me to break our "do not talk about quantum computing before 9am"-rule so many times.

Table of Contents

List of Tables

List of Figures

Chapter 1

Introduction and motivation

1.1 Quantum computing

Alan Turing invented the programmable computer in 1936 [1]. The invention of the point-contact transistor by Bardeen, Brattain and Shockley [2], in 1947, made it possible to produce smaller and more affordable computers, preparing the mass production era we are in today. We have been using these classical computers -they work out computations using classical physics- for more than 50 years now and decades of innovation have turned them into portable user-friendly everyday devices. Yet, the computers we use now still rely on the model described by Turing close to 80 years ago. Of course, calculations are much faster now (billions of operations every single second) while cheap memory and wide networks have opened the door to new uses.

Roughly speaking, if we could run the same program on two computers manufactured 50 years apart, the algorithm would require the same number of elementary operations on both. On the most recent one, the computation time would be much shorter, though, simply because present-day processors can perform billions of elementary operations per second.

Most of the improvements we find in recent computers can indeed be accounted for by the incredible number of transistors we are now able to put on a microchip. In the

1960s, a famous "law" claiming the number of transistors per surface unit would come to double every 18 months was foreseen by Moore and named after him. This pace was kept up until today, but classical computers designers are now approaching the limits of miniaturization. Not only the smaller they go, the harder it gets in terms of engineering, but they are reaching scales at which classical physics will not be sufficient to predict what is happening in the electronic circuits anymore: the quantum mechanical behaviour of electrons in the circuits have to be taken into account.

While for classical computers, this quantum mechanical behaviour can be considered undesirable (because it is not under control), Feynman was one of the first to suggest the idea of actually using the quantum properties of some systems to process information and work out computations [3]. The theory of quantum mechanical computers has since grown into a worldwide field of study, and first realizations are on their way.

Encoding information in quantum systems is indeed very different from its classical counterpart. While classical bits have to be either 0 or 1, quantum bits (qubits) can be a superposition of these two. Superposition is one of the reasons quantum computers will be able to run some algorithms exponentially faster than classical computers. Indeed, it allows the user to send all the possible inputs to a system in parallel, while classically those requests would have to be sent one after the other. This is, for instance, a key in Grover's fast search quantum algorithm [4]. But superposition is not the only phenomenon to account for the leap expected from quantum computers: entanglement is another one. Entanglement has no classical counterpart and is the sharing of an inseparable state between several quantum systems. The use of entanglement in quantum information processing is already well-known for allowing superdense coding and teleportation.

The most famous and impressive algorithm designed for quantum computers so far is probably the factoring algorithm [5]. While most of today's cryptography systems rely on the difficulty of factoring large numbers [6], which becomes exponentially harder with the size of the number to factorize, in a world with quantum computers, such a problem could actually be handled in a reasonable execution time.

1.2 Challenges of a physical implementation

Quantum states are known to be extremely fragile. The laws they obey can be counter-intuitive, and if we never observe any quantum effect of any kind in our everyday life it is because observing the quantum behaviour of a system requires an extremely stringent environment.

In order to help identify potential physical realizations of quantum processors, DiVicenzo listed 5 requirements which have now become a standard set of criteria when it comes to physical implementation of qubits [7].

1. A scalable physical system with well characterized qubits.

2. The ability to initialize the state of the quibit to a simple, identifiable state ($|00...\rangle$, ...).

3. A "universal" set of quantum gates.

4. Decoherence times much longer than the gate operation times.

5. A qubit-specific measurement capability.

There are many different ways to physically implement qubits and store quantum information. For example, isolating two energy levels in an Hydrogen atom could serve as a two-level system suitable to implement a qubit. As for macroscopic systems, neutron interferometers define a two-level system by distinguishing the two different paths that can be taken by a neutron.

Optical implementations are a leading candidate for the very long coherence times of the photonic quantum states. The quantum state can for instance be encoded as the polarization of a single photon, which involves well-known optics. Superconducting circuits are also used to implement qubits and allow the researchers to work with macroscopic system as opposed to much smaller systems with other technologies. On the other hand, decoherence is hard to remove in these so-called "artificial" quantum systems. In the recent

years, trapped ions (one of the first proposal for quantum computers [8]) have also been used successfully, for instance in a 14-qubit entanglement experiment [9].

Spin is an intrinsic quantum angular momentum that some elementary particles carry. Spin-$\frac{1}{2}$ particles form a natural quantum two-level system and are then used in many systems as qubits. Indeed, electron spins can be confined inside quantum dots or result of an ensemble of unpaired electrons in a crystal. Nuclear spins have a long history as probes of matter in the field of nuclear magnetic resonance, and can be manipulated directly with radio-frequency (RF) fields, or indirectly via coupled electron spins.

1.3   Towards implementation of quantum algorithms

1.3.1   Main obstacles

In classical computers, the "state" of the bits is usually physically implemented as a voltage. Distinguishing between a 0 and a 1 then reduces to setting thresholds on said voltage. For instance, it can be considered that any voltage between 0V and 1V should be understood as a 0, any voltage between 2V and 3V as a 1, while a voltage between 1V and 2V could be seen as a transcription error.

As far as quantum computers are concerned, even a small alteration of the information contained in a qubit is very likely to affect the final result of a computation. Yet, the threshold theorem tells us that the probability of error of a quantum algorithm using a large enough number of qubits can be made arbitrarily small provided the error probability for each single qubit is maintained under a certain threshold and quantum error-correcting codes are applied and using an amount of resources that scale polynomially to the size of the problem that one wants to solve.

All the physical implementations of qubits do not have to face the same obstacles in order to handle complex algorithms. Indeed, the probability to have an error on a single qubit as well as the pace at which errors can happen is related to the characteristic decoherence times of the considered system: reaching fidelities needed for fault-tolerant quantum operations is really technology dependent. A good knowledge of the errors likely

4

to happen to the system then allows one to use the threshold theorem to its maximum advantage: at regular intervals, quantum error-correcting procedures can be performed but one has to keep in mind that those procedures are subject to errors as well!

1.3.2   Quantum error-correcting codes

As a consequence, similarly to classical computers, quantum computers will have to be able to handle errors. Quantum error-correcting codes aim at protecting the information contained in a state, especially against the imperfections of the control system and, more than anything else, against the decoherence brought about by the interactions with the environment.

The theory of quantum error-correcting codes has been worked out [10] and relies on the encoding of the state to protect into a larger one. The idea[1] is the following: if a known error is likely to happen to a qubit, a quantum circuit can be designed to protect the information against this error by adding some qubits initialized in the $|0\rangle$ state (called *ancilla* qubits) to the original qubit. In addition of protection of the quantum information contained in the original qubit, the ancilla qubits will end up carrying information about the error that occurred.

Quantum error-correcting codes have been implemented in liquid-state [11] [12] [13] NMR, solid-state [14] NMR and trapped ions [15] [16]. More recently, implementations have been successful with superconducting circuits [17] and in NV-centres [18].

We believe that the implementation of quantum error-correcting codes in hybrid (or *heterogeneous*) quantum systems will open the path to implementation of quantum information processing in larger and more complex systems. Electron-nuclear systems are well suited for such implementation too, since the nuclei have long decoherence times but slow direct control, whereas the electron can give fast control (as an actuator) and also gives a way to reset to $|0\rangle$ via spin-lattice relaxation. Similarly to the revolution it has been for classical computers in the 1940s, it will set one more important step towards the realization of quantum computers.

---

[1]Chapter 6 goes further in the details of quantum error correction.

1.4 Layout of the thesis

Throughout this thesis, I will explain how and why we are going towards implementation of quantum algorithms using electron and nuclear spins in single crystals. Contextualizing the work I have taken part in, in the ESR project with Dr. Robabeh Rahimi Darabad and Daniel K. Park, I will highlight my main contributions, which are the Hamiltonian determination of our quantum system and how to use this knowledge in order to obtain an optimal experimental setup for the quantum algorithms we plan to implement. My goal is to convince the reader that using this knowledge, simulations programs we wrote and the procedure for optimal orientation we set up, we will soon successfully implement interesting quantum algorithms in a system potentially offering 5 qubits.

First of all, I will present the solid-state samples used in this work in Chapter 2. The crystal structure will be presented and our ESR characterization method will be discussed and reviewed. Chapter 3 presents the simulation programs used to confirm the characterization results but also to plan the results of the different algorithms we implemented or will implement for future work. The design of the experimental part of this work is shown in Chapter 4. The two last parts of this thesis will focus on our proposals for implementation of algorithmic cooling (Chapter 5) and quantum error correction (Chapter 6). Indeed, one method to dynamically provide the system with fresh ancilla qubits consists of multiple rounds of heat-bath algorithmic cooling. We will then present a method to refresh the ancilla qubits at the necessary pace and open the way to the implementation of quantum error-correcting codes using electron and nuclear spins in single crystals.

Chapter 2

Sample characterization

2.1 Malonic Acid

The samples we used in our experiments are malonic acid crystals. Malonic acid is a dicarboxylic acid with chemical formula $CH_2 (COOH)_2$ which has proved to be an excellent testbed for quantum information processing and has been studied a lot in the past decades [19] [20] [21] and more recently to entangle an electron spin and a nuclear spin [22]. Malonic acid single crystals can be grown and are stable at room temperature, where their structure is triclinic. The sample preparation is revealed in section 2.1.1 while the details of this structure are described in section 2.1.2.

2.1.1 Nomenclature and preparation

In this project, we worked with various slightly different molecules of malonic acid. To grow those different kinds of malonic acid crystals, we had to order *labelled* raw material in the first place. Each malonic acid molecule contains 3 carbon atoms. The natural abundance of carbon isotopes is close to 99% for ^{12}C and 1% for ^{13}C. Labelling is the replacement of the spinless ^{12}C by spin-$\frac{1}{2}$ ^{13}C. Our molecule then offers more nuclear spins for quantum control and implementation of quantum information processing. Depending
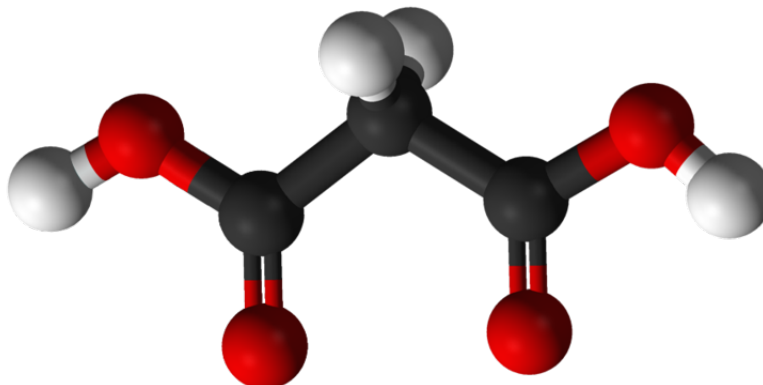
Figure 2.1: Spatial representation of a malonic acid molecule. The black spheres denote the 3 carbons, the red ones indicate the positions of the oxygens and the white ones represent the hydrogens. The two $COOH$ carboxylic groups appear on the sides while the central CH_2 methylene group connects them in the middle. The distance between the hydrogens of the carboxylic groups is close to 5Å. For nomenclature, we label the 3 carbons 1, 2 and 3 respectively, from left to right.

on the situations, it was easier for us to work with one of the types listed in table 2.1. For instance, we tried and perfected our orientation procedures on unlabelled malonic acid crystals before applying them to more expensive labelled crystals. But cost was not the only reason we sometimes chose to work with different samples: the difficulty of tensors extraction from continuous-wave (CW) measurements of fully-labelled malonic acid made us work with laterally-labelled crystals instead. We also performed CW measurements on deuterated[1] unlabelled malonic acid to estimate linewidth improvements we can expect for future works.

---

[1]In those molecules, the ^1H hydrogen atoms are replaced by ^2H deuteriums.

For all the different malonic acid molecule versions, the growth procedures are similar. A solution is obtained by dissolving existing crystals in a solvent (usually water[2]). The crystal growth is then made possible by controlling the evaporation rate of the solvent.

The final steps of the sample preparation were designed to get the controllable electron spin in the molecule. This unpaired electron is obtained after γ or X-ray irradiation of the sample for a precise duration (from a few of minutes for the former to a couple of days for the latter, the dose needed being 2kGy). Inducing defects in the crystal structure by destroying the carbon-hydrogen bonds results in the formation of radicals. Most of these radicals are not stable and a 60°C hot 24-hour long annealing was necessary to end up with stable radicals only.

---

[2]The solvent is actually not always water. Crystals can be grown in pure ethanol and will usually be larger but will then not be single crystals. To obtain nice single crystals, we ended up using a mix of water and ethanol as our solvent. Also, growing deuterated malonic acid crystals requires the use of heavy water (^2H_2O) instead of water (^1H_2O).

Table 2.1: Nomenclature and skeletal representations of regular and irradiated malonic acid molecules.

Molecule	Regular form	Irradiated form
Malonic acid (MA)		
Centrally-labelled malonic acid $(2 - ^{13}C$ MA$)$		
Laterally-labelled malonic acid $(1, 3 - ^{13}C$ MA$)$		
Fully-labelled malonic acid $(1, 2, 3 - ^{13}C$ MA$)$		

2.1.2 Crystal structure

The crystal structure of malonic acid has been studied throughout the past decades [23] [24]. The space group was found to be $P\bar{1}$ with $Z = 2$, meaning that each unit cell of the crystal contains two molecules related by a centre of symmetry.

Malonic acid crystal have a triclinic structure. To define their unit cell, we need 3 vectors $\vec{a}$, $\vec{b}$ and $\vec{c}$, including their lengths and respective orientations to one another. Hence the definition of $\alpha = \left(\vec{b}, \vec{c}\right)$, $\beta = (\vec{a}, \vec{c})$ and $\gamma = \left(\vec{a}, \vec{b}\right)$
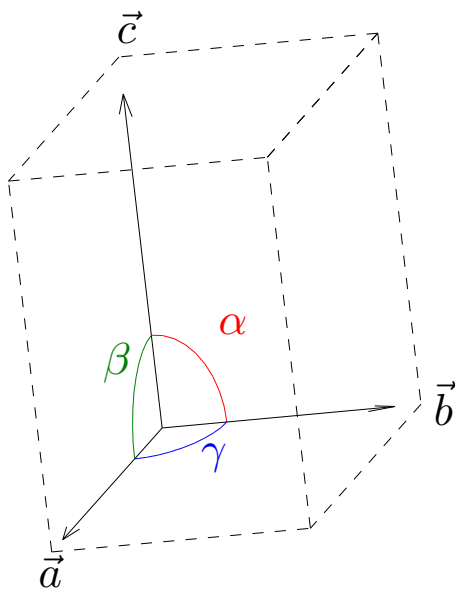
Figure 2.2: Malonic acid triclinic unit cell. The three vectors $\vec{a}$, $\vec{b}$ and $\vec{c}$ defining the unit cell form a direct basis and are represented as black arrows. The three angles α (red), β (blue) and γ (green) complete the definition of the unit cell.

The most recent structure results were published in 1994 by Jagannathan et al. [25].

These results are consistent with the structure Dr. Jalil Assoud (Dept. of Chemistry, University of Waterloo) is able to determine using a Bruker X-ray diffractometer.

Table 2.2: Malonic acid unit cell as published in 1994 by Jagannathan et al. and measured in 2014 by Dr. Jalil Assoud. Both are determined at T = 298K.

Jagannathan et al. [25]					Dr. Jalil Assoud			
a	5.156 Å	α	71.48°		a	5.16 Å	α	71.47°
b	5.341 Å	β	76.12°		b	5.33 Å	β	75.95°
c	8.407 Å	γ	85.09°		c	8.39 Å	γ	84.92°

Note that it is important for us to consider the first results published for the unit cell parameters of malonic acid because the first Hamiltonian determination publications (for centrally-labelled malonic acid) were using them. In particular, the eigenvectors direction cosines of the hyperfine tensor for the hydrogen have been published in that frame. These are essential for us to determine the optimal orientation to ensure the success of our implementations of quantum algorithms (see section 4.2 for more details).

2.2 Hamiltonian extraction

2.2.1 Mathematical model for Hamiltonian extraction

When dealing with quantum mechanical systems, the best characterization is usually the determination of the Hamiltonian of the system. The Hamiltonian is the energy operator of the system and in hybrid electron-nuclear spins-$\frac{1}{2}$ systems, it involves different types of interactions.

Because all the spins in our system are spins-$\frac{1}{2}$, when placed in a $\vec{B}_0 = B_0\hat{z}$ magnetic field, every type of spins will be given two possible levels of energy. This is called the *Zeeman splitting*. Apart from the Zeeman splitting, every spin interacts with every other, meaning the Hamiltonian of our system contains electron-nuclear and nuclear-nuclear spins
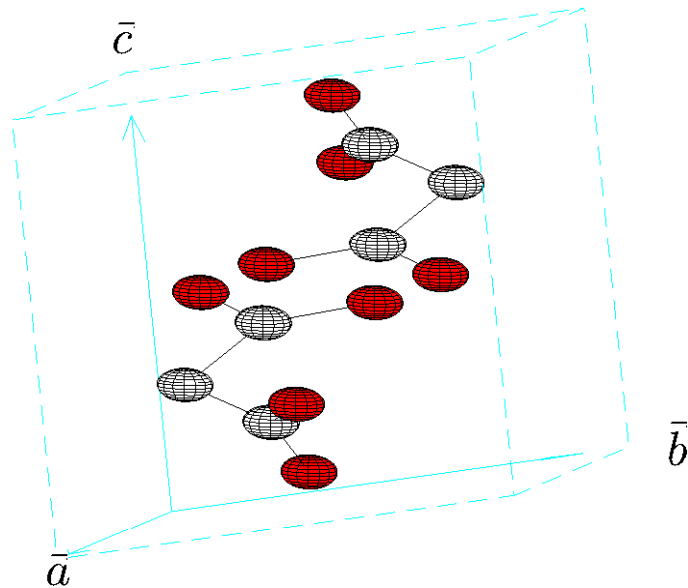
Figure 2.3: Malonic acid molecules in the unit cell. The positions of the atoms in each molecule has been published by Goedkoop and MacGillavry [24]. We also know that there are two molecules per unit cell related by a centre of symmetry, making them magnetically equivalent. The black spheres denote the positions of the carbons while the red ones show the position of the oxygens.

interaction terms. All the examples in this chapter will be taken from our extraction of the Hamiltonian for laterally-labelled malonic acid, which offers one electron spin and three nuclear spins: one hydrogen ^1H and two ^{13}C carbons.

Considering the usual strengths of the nuclear-nuclear spins interactions (0.1 to 10 kHz), we decided to neglect them, which is a common assumption when working with hybrid spins-$\frac{1}{2}$ systems.

Eventually, the Hamiltonian of the system we considered under those assumptions only contains the Zeeman splitting terms for each species of spins as well as the electron-nuclear spins interaction, called *hyperfine interaction* or *hyperfine splitting* - usually denoted by a

tensor $\vec{A}$. If we have a system with one electron spin and K nuclear spins (usually referred to as "1e-Kn" system) - see Appendix B for more details about the electron $\hat{S}$ and nuclear $\hat{I}_n$ spin operators notations:

$$\hat{H} = \frac{\mu_b}{h}\vec{B}_0 \cdot \vec{g} \cdot \hat{S} + \sum_{n=1}^{K}\omega_{I,n}\hat{I}_{n,Z} + \sum_{n=1}^{K}\hat{S} \cdot \vec{A}_n \cdot \hat{I}_n \qquad (2.1)$$

Where $\omega_{I,n} = -\gamma_n\|\vec{B}_0\|$ is the nuclear Zeeman splitting (proportional to $\|\vec{B}_0\|$).

$$\text{with :} \begin{cases} \mu_B & : & \text{Bohr magneton (constant)} \\ h & : & \text{Planck constant} \\ \vec{B}_0 & : & \text{external magnetic field} \\ \vec{g} & : & \text{g-tensor} \\ \gamma_n & : & \text{gyromagnetic ratio for nuclear spin } n \text{ (constant)} \\ \vec{A}_n & : & \text{hyperfine tensor for nuclear spin } n \end{cases}$$

To have a complete knowledge of this Hamiltonian for our system, we then need to determine the $\vec{g}$-tensor as well as the $\vec{A}_n$ hyperfine tensors. The procedure will be the same for all the tensors: using the orientation dependence of a *scalar parameter v*, we will be able to measure the coefficients of a certain tensor, that we call $\vec{\Gamma}$ and which is related to the tensors we are looking for. Table 2.3 relates the parameter v and the $\vec{\Gamma}$ calculated depending on the tensor ($\vec{g}$-tensor or hyperfine tensors) we want to extract. Notice that we always expect $\vec{\Gamma}$ to be symmetric which leaves us 6 coefficients to determine it fully.

$$\vec{\Gamma} = \begin{bmatrix} \Gamma_{xx} & \Gamma_{xy} & \Gamma_{zx} \\ \Gamma_{xy} & \Gamma_{yy} & \Gamma_{yz} \\ \Gamma_{zx} & \Gamma_{yz} & \Gamma_{zz} \end{bmatrix} \qquad (2.2)$$

If we call $X - Y$ the plane being considered (with Z pointing up) and set X to be initially aligned with the external magnetic field (thus defining θ as the angle between the magnetic field and X to be 0 for the first measurement), the theory [26] gives us the following orientation behaviour for v^2:

Table 2.3: Parameter to consider for the determination of the hyperfine and $\vec{g}$-tensors.

Tensor	Parameter to measure	Tensor determined
$\vec{g}$	$v = g$	$\vec{\Gamma} = \vec{g} \cdot \vec{g}$
$\vec{A}_n$	$v = g A_n$	$\vec{\Gamma} = \vec{g} \cdot \vec{A}_n \cdot \vec{A}_n \cdot \vec{g}$

$$v^2(\theta) = \Gamma_{xx} \cos^2 \theta + \Gamma_{yy} \sin^2 \theta + \Gamma_{xy} \sin 2\theta \tag{2.3}$$

From table 2.3 and the orientation behaviour shown in equation 2.3, we see that we need to measure the orientation dependence of a g and an A_n *scalar values* in more than one plane. Actually, for a complete study, we need to measure those values (and their orientation dependence) in 3 non-parallel planes. Our extraction model relies on two assumptions: the 3 planes of measurements are mutually non-parallel, and the axis of the rotation to go from one to the other actually belongs to both planes. Our algorithm also assumes that the angle step between each measurement in one plane is constant. We estimate our experimental angle precision to be $\pm 1°$.
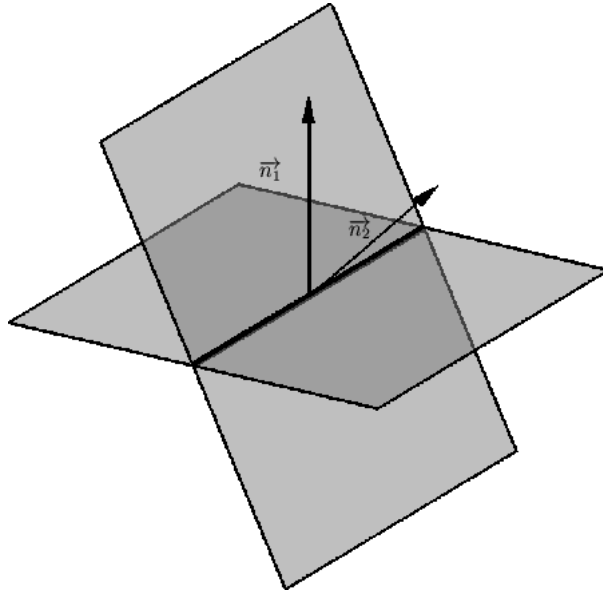
Figure 2.4: Two non-parallel planes and their intersection. The two surfaces are characterized by their normal vector and intersect along a line. This line is one the axes of rotation to go from one plane to the other. We tried to use this axis to go from one plane to an other one.

2.2.2 Orientation study of the CW ESR peaks positions

In CW spectroscopy, a spectrometer sends pulses at a fixed frequency sweeping the magnitude of the magnetic field. Peaks appear for particular values of the magnetic field for which transitions between energy levels the system can occupy are driven. The extraction procedure relies on the orientation study of the allowed transitions peaks positions in the CW ESR spectra. From the orientation trajectories of these peaks, we are able to measure the g and A_n values as a function of the orientation of the magnetic field.

A one electron spins - K nuclear spins system (abbreviated "1e-Kn" system) contains $K + 1$ spins-$\frac{1}{2}$, hence its Hamiltonian is a $(K + 1) \times (K + 1)$ matrix and there are $K + 1$ eigenenergies. In CW ESR spectroscopy, the peaks that will appear correspond to the transitions flipping the electron spins. Among those, some transitions, called *allowed transitions*, will flip *only* the electron spin. The *forbidden transitions*, on the other hand, will

flip the electron spin along with at least one nuclear spin. It can easily be understood from the energy diagram in figure 2.5 that the number of allowed transitions in a 1e-Kn system is 2^K. Notice the transition probability is much higher for the allowed transitions and this is revealed in the ESR spectrum in terms of amplitudes of the peaks. Since forbidden transitions are very difficult to observe, this study only uses the allowed transitions peaks to determine the tensors in the Hamiltonian.
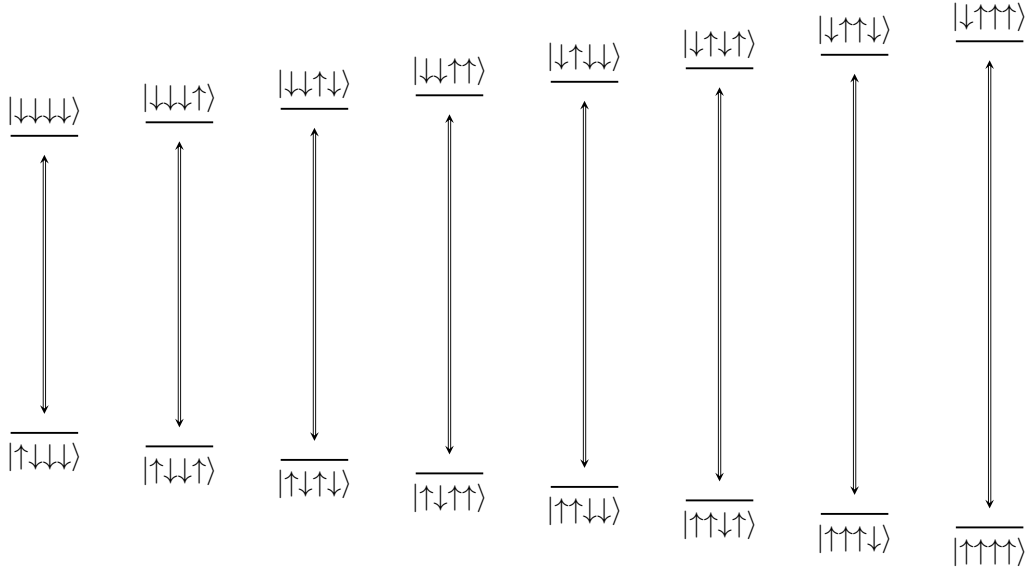
Figure 2.5: Energy diagram of a 1e-3n system with allowed ESR transitions. The spin states are in the $|e^-, H, C_1, C_2\rangle$ order. Each spin qubit is a two-level system where the two levels are denoted by $|\uparrow\rangle$ and $|\downarrow\rangle$. The state labelling can be done by replacing $\uparrow$ by 1 and $\downarrow$ by 0. Then, the states can be read as binary numbers. For example, in the top-left corner, we have $|\downarrow\downarrow\downarrow\downarrow\rangle = |0000\rangle = |0\rangle \otimes |0\rangle \otimes |0\rangle \otimes |0\rangle = |0\rangle$. Similarly, $|7\rangle = |0111\rangle = |\downarrow\uparrow\uparrow\uparrow\rangle$, for instance.

To measure the g-value and the hyperfine splittings A_n needed for the tensors extraction, it is important to understand the structure of a CW ESR spectrum. If we measure the CW ESR spectrum of an electron spin alone, we will obtain one peak for a specific value of the magnetic field called the centre field B_{centre}. The centre field is related to the g-value by the resonant condition (in which the frequency of the spectrometer, ν, is fixed):

$$h\nu = g\mu_B B_{\text{centre}} \tag{2.4}$$

Adding one nuclear spin n_1 to the system will double the number of peaks: we obtain two "sub-spectra", one shifted by $\frac{A_1}{2}$ to the left, one shifted by $\frac{A_1}{2}$ to the right. Here, A_1 is the observable hyperfine splitting due to n_1, the one we need to determine the $\vec{A}_1$ tensor. Similarly, adding one more nuclear spin n_2 will continue this division process: the left and right sub-spectra will be divided into four sub-sub-spectra shifted by $\frac{A_2}{2}$ to the left and to the right. Notice that, from the way the CW ESR spectrum is structured, and as the name suggests, the centre field is the center of symmetry of the spectrum, as shown in figure 2.6.
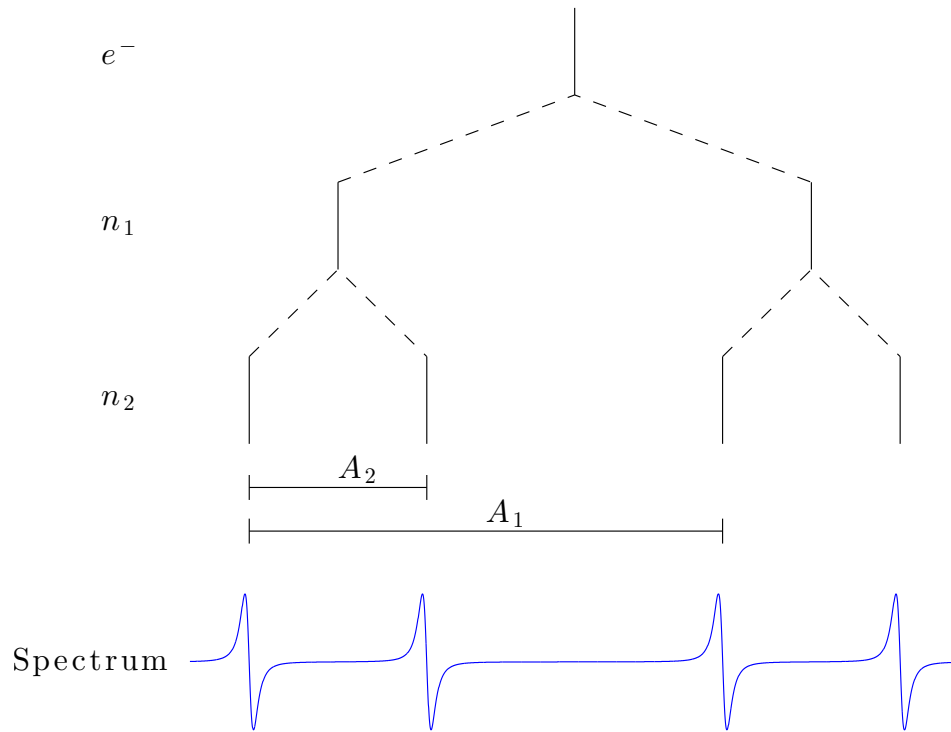
Figure 2.6: Structure of the CW ESR spectrum. The positions of the allowed transitions peaks follow a pyramidal structure, each splitting adding new leaves to the tree.

From this picture, we can understand how to use the information contained in each spectrum to measure the observed hyperfine splittings for each nuclear spin as well as the g-value. Since the peaks will "move" with the orientation of the magnetic field with respect to the crystal, their positions can overlap or cross, making the analysis a little tricky.

However, one splitting that is usually easier to measure is the largest one (i.e. A_1) because it divides the final spectrum into two sets of peaks usually clearly distinguishable. Having a look at the general peaks trajectories in each plane is usually enough to relate a measured spectrum to its expected structure.

2.2.3 CW spectrometer and measurements

The usual way to go through this orientation study requires a goniometer, but we worked on Hamiltonian determination relaxing the need for such a tool. We chose to work out measurements in 3 non-parallel planes, trying to get them mutually orthogonal to each other. In each of these 3 planes, for our study of laterally-labelled malonic acid, we measured 90 spectra of the sample[3].

We use a Bruker X-band CW spectrometer belonging to David Cory's group, whom we thank a lot. The crystal is hosted by a Stycast 1266 box engineered to be as cubic as possible (making it easy for us to identify the 3 planes we wanted to measure). This box is then placed inside a sample tube allowing us to make sure the sample is centred in the magnet. In order to measure spectra with different orientations of the magnetic field with respect to the crystal, the sample tube is rotated by some angle between every measurement, using a graduated plate as a reference.

Let us take the example of our Hamiltonian determination for laterally-labelled malonic acid. For each measurement, the range of magnetic fields applied was 3295G to 3395G. We performed 16 scans to average the noise out for every single spectrum measured. Our results files contained the measured spectrum with 4000 points -which corresponds to a field step of 0.025G-, as well as the frequency of the spectrometer, which had to be fine tuned after a few measurements. Between every measurement, the sample tube was rotated clockwise by 2°.

On our measurements, it appeared that the hyperfine coupling between the electron and each of the two lateral carbons were too close to be distinguished from one another. Thus, instead of observing 8 peaks, we only see 6: two peaks appearing (with square markers on figure 2.12) overlap for all the orientations.

---

[3]In theory, 3 infinitely precise measurements in each plane are sufficient. Collecting more data allowed us to get results robust against systematic error and noise.
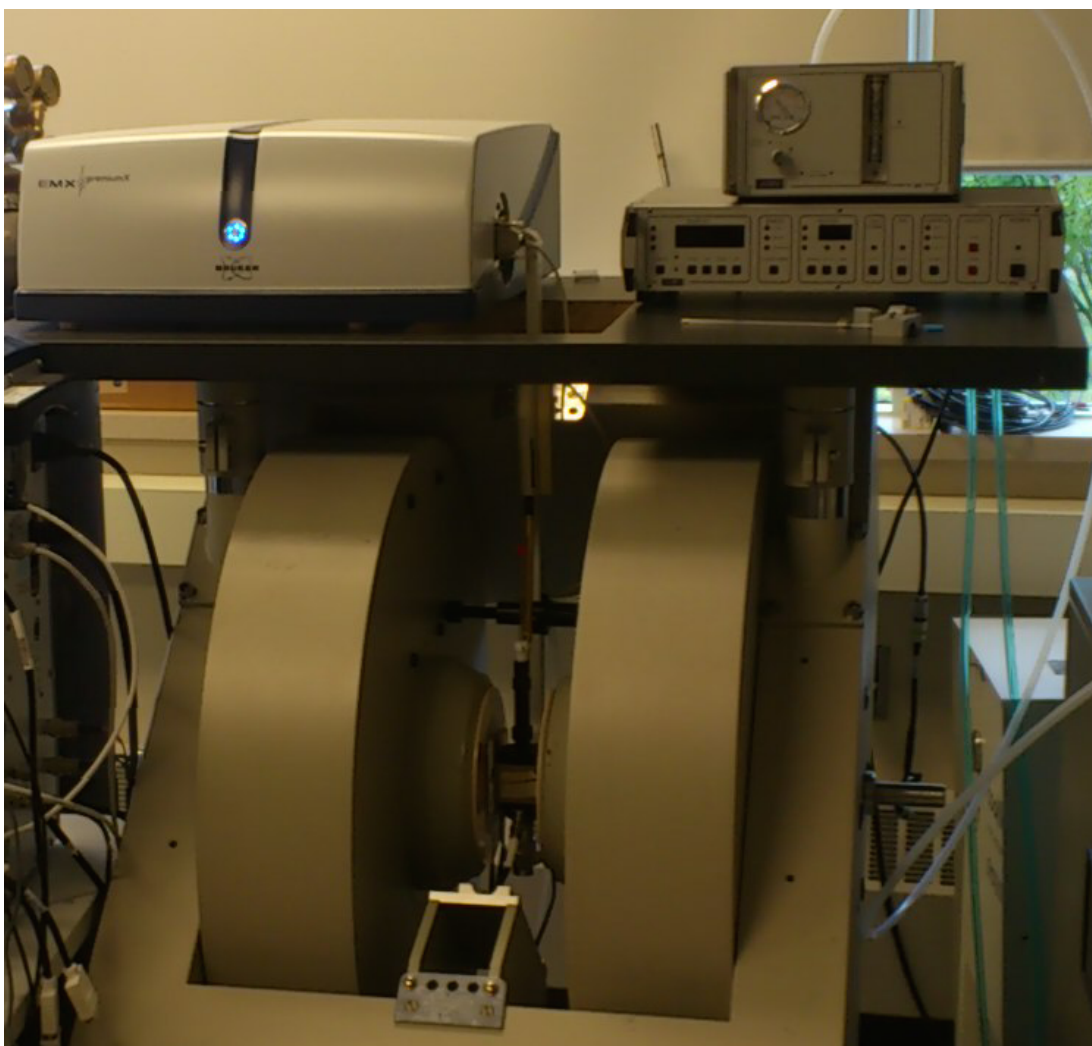
Figure 2.7: Bruker X-band CW spectrometer. The two cylinders are the poles of the electromagnet. The sample is place between them, where the magnetic field is created, in the cavity with a resonator. The boxes in the top-right corner are respectively a temperature-meter and a pressure-meter (on the top). They are used to measure the temperature and regulate the flow of liquid Helium or liquid Nitrogen when we do low-temperature experiments. The box in the top-left corner is the wave-generator. At the very back on the right, we can see the water chiller used to cool the electromagnet.
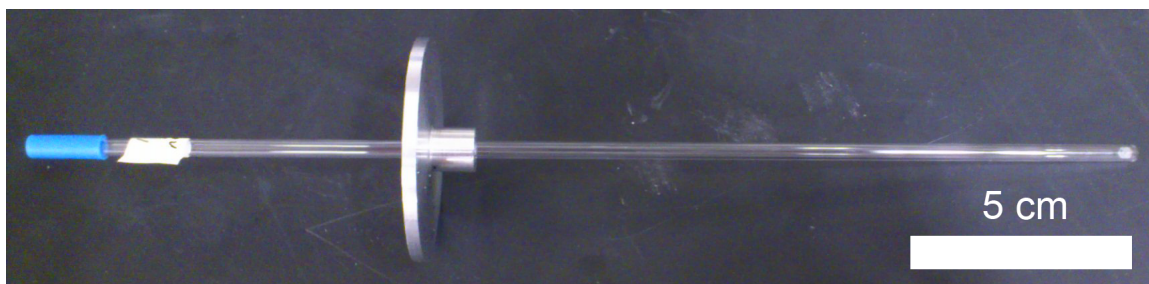
Figure 2.8: The sample tube in which lays the Stycast box hosting the crystal. This is simply a standard sample tube for the Bruker CW spectrometers. The tube is 25cm long with a diameter of 4.1mm.
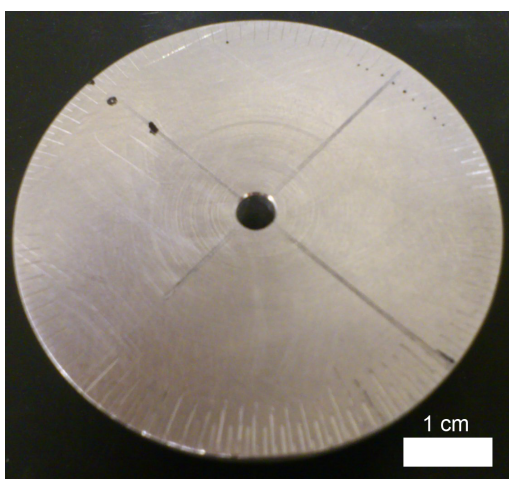
(a) Graduated plate for CW measurements.

(b) Stycast box for crystal orienting.

Figure 2.9: The graduated plate (a) we used shows two types of marks: long ones every 4° with short ones in between. It was machined by the University of Waterloo machine shop. The plate has a diameter of 5.2cm. We used a special mould to make the Stycast box (b) as square as possible, making it much easier to manipulate the crystal and its very irregular shape. The box has an estimated side length of 3mm.
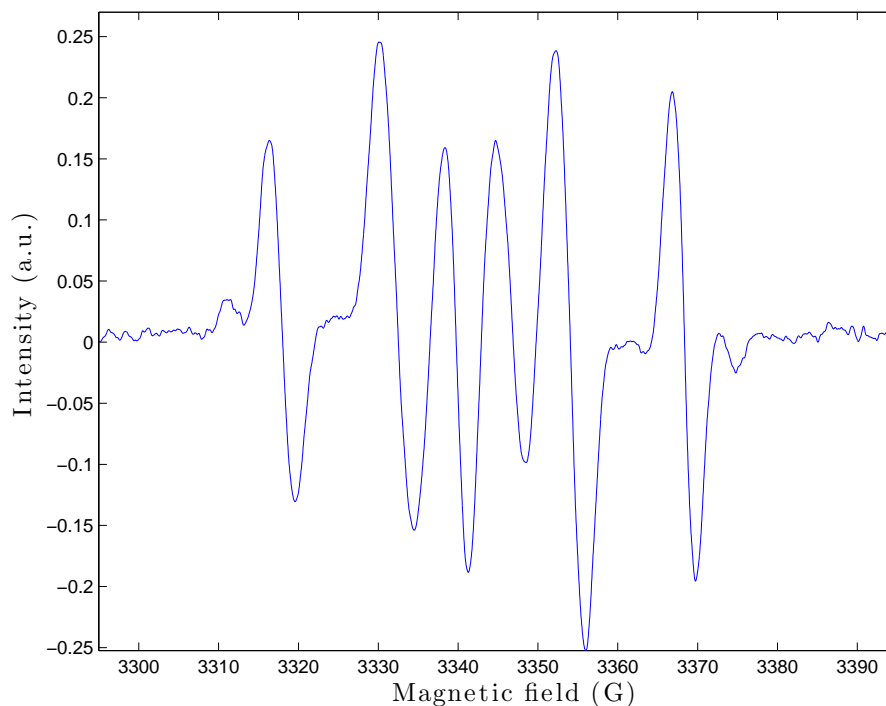
Figure 2.10: Example of a CW ESR spectrum we measured for laterally-labelled malonic acid. The signal detected is the first derivative of the CW ESR absorption spectrum. Without overlap and if the peaks are far enough from one another (compared to their linewidth -here around 14MHz), the amplitudes of the peaks are expected to be symmetric with respect to $y = 0$. The spectrum itself is symmetric with respect the centre field (here approximately 3340G).

To extract the positions of the allowed ESR peaks on each spectrum, we had to do some processing on the signals we got from the spectrometer. First of all, we know that the peaks are expected when the signal crosses $y = 0$. Starting from all the zeros of the system, we can then isolate the possible peak positions, for example by adding a constraint on the sign of the derivative of the signal at the considered point, expected to be negative. Eventually, we obtain a first guess of the positions and amplitudes of the peaks, as well as their linewidth. This iterative process is terminated with our optimization program, which

23

returns the optimal positions and amplitudes for each signal, allowing us to plot the plane overview for the trajectories of these peaks.

To observe this, we plot the spectra measured for consecutive orientations of the magnetic fields with respect to our crystal in one plane. On the plane overview, it then appears clear that we observe two different hyperfine splitting values. The large one splits the spectra into two sets of curves clearly distinguishable: the first manifold is denoted by green curves in figure 2.12 while the second manifold is denoted by the purple curves. This splitting is due to the central hydrogen. In each manifold, we can see that the curves with a square marker correspond to overlapping peaks coming from the lateral carbons. From this observation, we can then measure the g-value along with the A_H and A_C values.
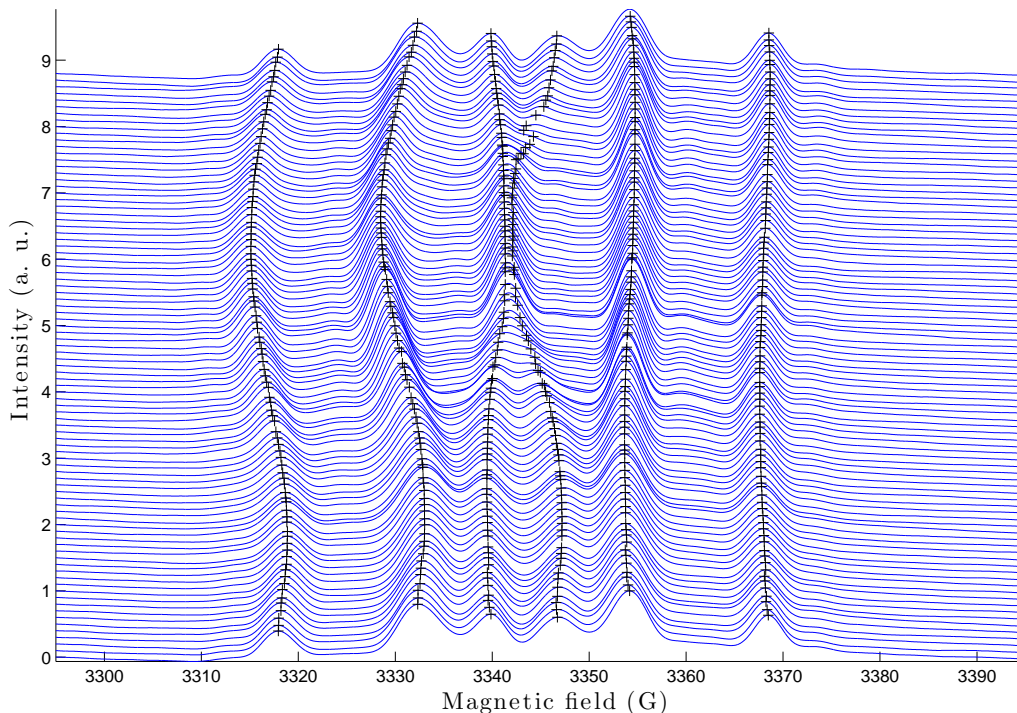
Figure 2.11: Spectra and allowed transitions peak positions for equally-spaced consecutive angles in plane 1 for our measurements on laterally-labelled malonic acid. The plot shows absorption spectra, which are obtained by integrating the spectra returned by the spectrometer. The black crosses are the optimal peak positions determined with our algorithm.
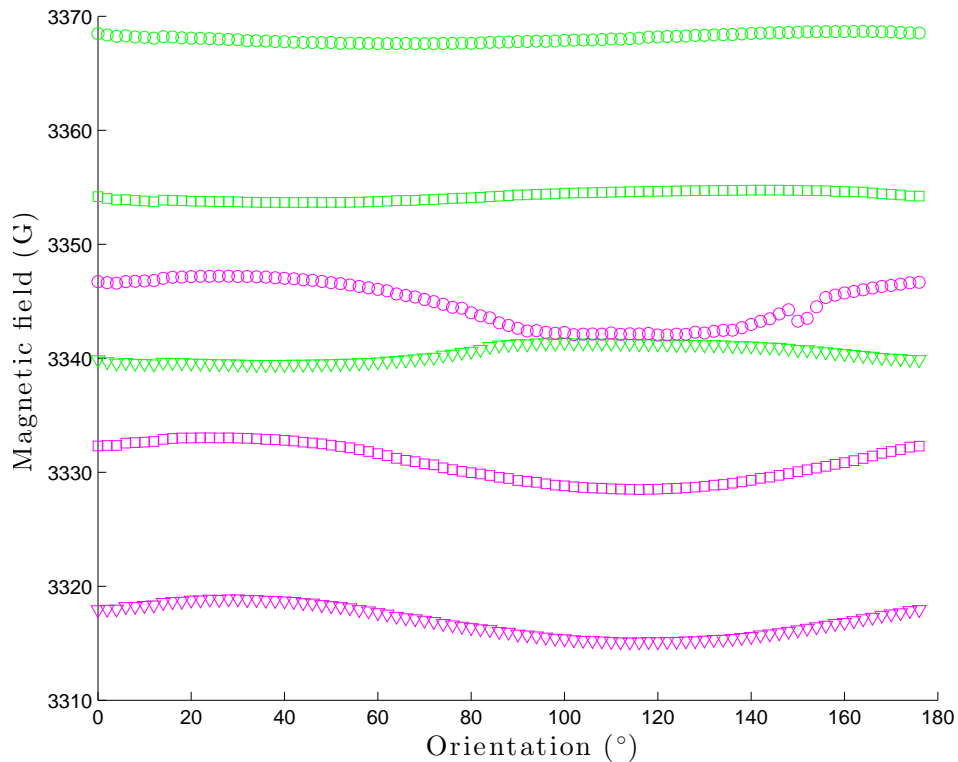
Figure 2.12: Allowed transitions peaks positions in plane 1 for our measurements on laterally-labelled malonic acid. The figure reveals the orientation dependence of those peaks alone. Two hyperfine splittings can be observed: a large one between the curves of different colours sharing the same marker, and a small one between the curves of same colours. This tells us that the curves denoted by a square marker are the result of an overlap between two peaks, as the single spectra revealed (the amplitude of those overlapped peaks was around twice as large as the one of the other peaks).

2.2.4 Determination of hyperfine and $\vec{g}$ tensors

Using the peak trajectories in each plane, we are able to measure the orientation dependence of v, where the definition of v depends on the tensor we are extracting, as shown in table 2.3. If we provide our 3 planes with one axis system, X_1, Y_1, Z_1 for plane 1, and so on, we then expect an orientation dependence of v^2 *in this frame* (for instance) as given by equation 2.3:

$$v^2(\theta) = \Gamma_{xx} \cos^2 \theta + \Gamma_{yy} \sin^2 \theta + \Gamma_{xy} \sin 2\theta \tag{2.5}$$

The key to determine the three coefficients of the $\vec{\Gamma}$ tensor that appear in this expression is to see this problem as a problem of algebra. Indeed, let us consider the vector space of infinitely differentiable functions of $[0, \pi]$ to $\mathbb{R}$, $C^\infty([0, \pi], \mathbb{R})$, and especially the subspace generated by $\{\cos^2 \theta, \sin^2 \theta, \sin 2\theta\} = \{f_1, f_2, f_3\}$.

It is easy to show that those three vectors f_1, f_2 and f_3 are linearly independent since $\forall (\lambda_k)_{k=1,2,3} \in \mathbb{R}$, $\sum \lambda_k f_k = 0 \Rightarrow \forall k \lambda_k = 0$. As a consequence, we can simply decompose our vector v^2 along this family of linearly independent vectors. This tells us that the coefficients Γ_{xx}, Γ_{yy} and Γ_{xy} are unique but what is more is that we know how to obtain them. Given a dot product on this vector space, denoted $\langle . | . \rangle$:

$$\langle v^2 | \, f_1 \rangle = \Gamma_{xx} \langle f_1 | \, f_1 \rangle + \Gamma_{yy} \langle f_2 | \, f_1 \rangle + \Gamma_{xy} \langle f_3 | \, f_1 \rangle$$
$$\langle v^2 | \, f_2 \rangle = \Gamma_{xx} \langle f_1 | \, f_2 \rangle + \Gamma_{yy} \langle f_2 | \, f_2 \rangle + \Gamma_{xy} \langle f_3 | \, f_2 \rangle$$
$$\langle v^2 | \, f_3 \rangle = \Gamma_{xx} \langle f_1 | \, f_3 \rangle + \Gamma_{yy} \langle f_2 | \, f_3 \rangle + \Gamma_{xy} \langle f_3 | \, f_3 \rangle$$

$$\begin{bmatrix} \langle v^2 | \, f_1 \rangle \\ \langle v^2 | \, f_2 \rangle \\ \langle v^2 | \, f_3 \rangle \end{bmatrix} = \begin{bmatrix} \langle f_1 | \, f_1 \rangle & \langle f_2 | \, f_1 \rangle & \langle f_3 | \, f_1 \rangle \\ \langle f_1 | \, f_2 \rangle & \langle f_2 | \, f_2 \rangle & \langle f_3 | \, f_2 \rangle \\ \langle f_1 | \, f_3 \rangle & \langle f_2 | \, f_3 \rangle & \langle f_3 | \, f_3 \rangle \end{bmatrix} \begin{bmatrix} \Gamma_{xx} \\ \Gamma_{yy} \\ \Gamma_{xy} \end{bmatrix}$$

$$\begin{bmatrix} \Gamma_{xx} \\ \Gamma_{yy} \\ \Gamma_{xy} \end{bmatrix} = \begin{bmatrix} \langle f_1 | \, f_1 \rangle & \langle f_2 | \, f_1 \rangle & \langle f_3 | \, f_1 \rangle \\ \langle f_1 | \, f_2 \rangle & \langle f_2 | \, f_2 \rangle & \langle f_3 | \, f_2 \rangle \\ \langle f_1 | \, f_3 \rangle & \langle f_2 | \, f_3 \rangle & \langle f_3 | \, f_3 \rangle \end{bmatrix}^{-1} \begin{bmatrix} \langle v^2 | \, f_1 \rangle \\ \langle v^2 | \, f_2 \rangle \\ \langle v^2 | \, f_3 \rangle \end{bmatrix}$$

We choose to use the natural dot product on our sub vector space V to calculate different components.

$$\forall \, u_1, u_2 \in V, \quad \langle u_1 | \, u_2 \rangle = \int_0^\pi u_1(\theta) u_2(\theta) d\theta \tag{2.6}$$

Since we made the assumption that the rotation axis between two planes is contained in both planes, we have two measurements in both planes giving exactly the same spectra,

corresponding to the alignment of this rotation axis with the external magnetic field. Thus, we can identify the labels of the measurements that are identical in the two planes and rename our X axis to be the axis of rotation (which means re-labelling our measurements). Since we know the three coefficients defining the orientation dependence of our different v parameters, we can choose the precision of this localization to any angle step we want. We considered $1°$ was a sufficient precision.
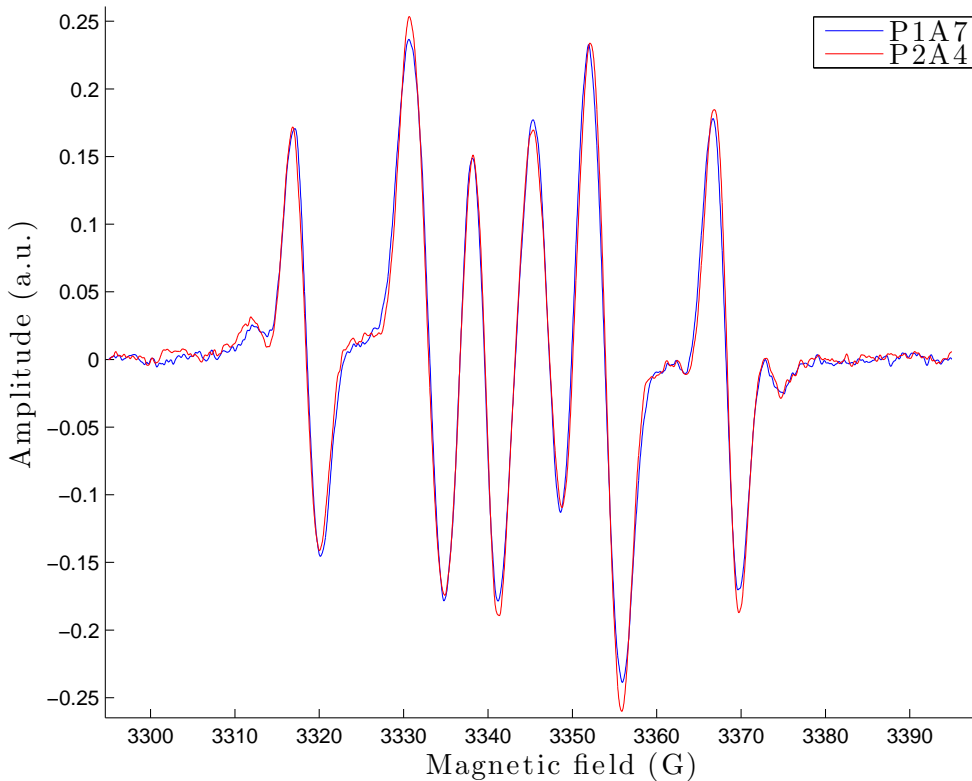
Figure 2.13: Identical CW ESR spectra in plane 1 (blue) and plane 2 (red) for our measurements on laterally-labelled malonic acid. "P1A7" is our eighth measurement in plane 1, while "P2A4" is our fifth measurement in plane 2. By looking at all the spectra measured in the two planes two by two, we can find the two corresponding with the same alignment of the magnetic field. This gives us the "coordinates" of the X-axis in plane 1 and plane 2.

To finish this characterization, we need two angles. We will call φ the rotation angle between plane 1 and plane 2 while ψ will denote the rotation angle between plane 2 and plane 3. These two rotations are along the X-axis, whose definition is changed as explained further. We then need to express the $\vec{\Gamma}$ tensor in 4 different frames: $\vec{T_1}$ is $\vec{\Gamma}$. $\vec{T_{21}}$ is $\vec{T_1}$ rotated of φ around X_{12} (axis of rotation between plane 1 and plane 2). $\vec{T_{22}}$ is $\vec{T_{21}}$ with the first measurement shifted to be aligned with X_{23} (axis of rotation between plane 2 and plane 3). $\vec{T_3}$ is $\vec{T_{22}}$ rotated of ψ around X_{23}. To complete this picture, we then need to define a new angle α which, contrary to φ and ψ, is *known* and characterizes the rotation to go from the frame of $\vec{T_{21}}$ to the frame of $\vec{T_{22}}$.

To summerize, we have:

$$\vec{T_1} = \vec{\Gamma}$$
$$\vec{T_{21}} = R_X(\varphi)^\dagger \cdot \vec{T_1} \cdot R_X(\varphi)$$
$$\vec{T_{22}} = R_Z(\alpha)^\dagger \cdot \vec{T_{21}} \cdot R_Z(\alpha)$$
$$\vec{T_3} = R_X(\psi)^\dagger \cdot \vec{T_{22}} \cdot R_X(\psi)$$

At the same time, using the data of the three planes, we can measure 3 coefficients of the tensors in each frame.

$$P1 : v^2 = T_{1,xx} \cos^2 \theta + T_{1,yy} \sin^2 \theta + T_{1,xy} \sin 2\theta$$
$$P2 - 1 : v^2 = T_{21,xx} \cos^2 \theta + T_{21,yy} \sin^2 \theta + T_{21,xy} \sin 2\theta$$
$$P2 - 2 : v^2 = T_{22,xx} \cos^2 \theta + T_{22,yy} \sin^2 \theta + T_{22,xy} \sin 2\theta$$
$$P3 : v^2 = T_{3,xx} \cos^2 \theta + T_{3,yy} \sin^2 \theta + T_{3,xy} \sin 2\theta$$

The fact that the three planes are mutually not orthogonal is now going to be critical because it explains how, using these 3 coefficients in each plane, we can calculate the whole tensor in the first frame. Indeed, here is how all the 12 coefficients measured are related to one another and allow us to write a system and solve it.

$$T_{21,xx} = T_{1,xx}$$

$$T_{21,yy} = T_{1,yy}\cos^2\varphi + T_{1,zz}\sin^2\varphi + T_{1,yz}\sin 2\varphi$$

$$T_{21,xy} = T_{1,xy}\cos\varphi + T_{1,zx}\sin\varphi$$

$$T_{22,xx} = T_{21,xx}\cos^2\alpha + T_{21,yy}\sin^2\alpha + T_{21,xy}\sin 2\alpha$$

$$T_{22,yy} = T_{21,yy}\cos^2\alpha + T_{21,xx}\sin^2\alpha - T_{21,xy}\sin 2\alpha$$

$$T_{22,xy} = T_{21,xy}\cos 2\alpha - (T_{21,xx} + T_{21,yy})\frac{\sin 2\alpha}{2}$$

$$T_{3,xx} = T_{22,xx}$$

$$T_{3,yy} = T_{22,yy}\cos^2\psi + T_{22,zz}\sin^2\psi + T_{22,yz}\sin 2\psi$$

$$T_{3,xy} = T_{22,xy}\cos\psi + T_{22,zx}\sin\psi$$

Let us analyse this set of equations. Some of those equations actually do not bring additional information: for example $T_{21,xx} = T_{1,xx}$ and $T_{3,xx} = T_{22,xx}$ were already known because we looked for X_{12} and X_{23} to satisfy those. Also, measuring the coefficients of $\vec{T}_{22}$ does not bring additional information because the coefficients of $\vec{T}_{21}$ as well as α are already known. They only serve as a double check.

Since Γ_{xx}, Γ_{yy} and Γ_{xy} have been measured directly by projecting v^2 in plane 1, at this stage, we have 5 unknowns left: Γ_{zz}, Γ_{zx}, Γ_{yz}, φ and ψ. At the same time, we have 4 equations (given by $T_{21,yy}$, $T_{21,xy}$, $T_{3,yy}$ and $T_{3,xy}$), which means that if we only want to extract one tensor, this method requires more data. In our case, though, we want to characterize a 1e-Kn system with $K \geq 1$. If we count the number of unknowns and the number of equations as functions of K (noticing such a systems requires us to determine $K + 1$ tensors), we can see that:

$N_{unknowns} = 6(K + 1) + 2$ since φ and ψ are the same for all the tensors.

$N_{equations} = 7(K + 1)$ counting the 3 direct measurements plus the 4 equations to solve.

In a nutshell, as long as we have at least one nuclear spin, this model of tensor extraction is valid. Of course, the system we have to solve is non-linear. Another difficulty is that our measurements are not infinitely precise, which means we stand no chance of actually mathematically solving this system. Instead, our algorithm uses optimization methods to get as close as possible to a solution simultaneously satisfying all the equations of this system.

2.3   Sample characterization results

2.3.1   Uncertainties and error bars

Estimation of the uncertainty on the diagonal coefficients of the tensors

The precision of our results is directly related to the precision with which we determine the coefficients in the tensors. We then had to work out the uncertainty on those coefficients. First of all, each experimental transition peak position is determined by some processing on the signals we got from the spectrometer. The rough detection is enhanced by a refined optimization taking into account the expected shape of the signal, completing this iterative process. Nevertheless, due to the linewidth of the peaks observed, there is a measurement error when we detect these positions. This type of error brings about vertical uncertainty. Furthermore, our method to manually rotate the sample, using a graduated plate, when collecting the data in each plane, is not perfect and gives us some horizontal uncertainty, due to experimental conditions.

However, we will not directly take into account these uncertainties and consider that the whole error is carried by the coefficient determination. Similarly, we will consider the values we determined for θ and φ as exact. Finally, we will consider that there is no error at all in our assumption that the rotation axis from plane to plane is rigorously contained in both planes.

From the tensors we determined, we can obtain the orientation dependance of the $v_{\text{sim.}}^2$ parameter for the $\vec{g}$-tensor and the hyperfine tensors and compare it to the measured $v_{\text{meas.}}^2$.

In each plane, we can then calculate the mean value of the error $E = v_{\text{meas.}}^2 - v_{\text{sim.}}^2$. We take the average of this error in the 3 planes as our uncertainty on the diagonal coefficients of the tensors we determined.

$$\Delta g^{exp.} = 0.013$$
$$\Delta A_H^{exp.} = 6.0 \text{ MHz}$$
$$\Delta A_{C_m}^{exp.} = 10 \text{ MHz}$$
$$\Delta A_{C_{1/2}}^{exp.} = 1.3 \text{ MHz}$$

In terms of orders of magnitude, our uncertainties are consistent with what can be expected. As said before, these uncertainties are overestimated because they contain all the kinds of errors in both the measurements and the determination processes. For instance, the measured line broadening of the peaks we observed in our measurements was 14MHz, which means our values for $\Delta A_H^{exp.}$, $\Delta A_{C_m}^{exp.}$ and $\Delta A_{C_{1/2}}^{exp.}$ are consistent, some of them being an order of magnitude smaller. These uncertainties look very important because they are overestimated. Our definition of Δ is an upper-bound of the actual error made in the coefficients determination and we are working on refining those results for future publications. Nevertheless, calculating the error bars using these uncertainties will allow us to see that they actually can account for the difference between our simulations and our measurements for all the orientations measured.

Error bars calculation

Since the tensor extraction procedure uses all the CW ESR data we have on our sample, we had no way to exploit additional data to work out error bars. We chose to use the uncertainty in the coefficients of our tensors to apply the Monte-Carlo method [27] [28][4]. With this method, we obtained more data by doing many simulations in order to obtain the distribution of our error. For every simulation, errors taken in a gaussian distribution

---

[4]I would like to thank my friend Mathieu Finas, from *École Centrale de Lille* for ideas and discussions on this topic.

of mean 0 and standard deviation Δ were added to the diagonal coefficients of our tensors. Using these "noisy" tensors, we can indeed simulate the positions of the allowed transition peaks and compare them to our main simulation (i.e. the one with the determined tensors, without the uncertainties).

From all those simulations we can measure the error distribution on the simulated positions. Since the physics simulated is linear, the error distribution is also gaussian, and we can easily calculate its standard deviation. The error bars are taken to be 2σ (σ being the standard deviation of the error distribution). Indeed, for gaussian distributions, more than 95% of the distribution is in the interval $[-2\sigma\ 2\sigma]$ when the mean is 0, like in our case.

Ideally, the number of simulations required to obtain convincing results is 10^n, where n is the number of variables in the system. In our case, we have three diagonal tensors, so we should try to run 10^9 simulations. However, each simulation takes slightly more than 1s, which means we would have to wait 32 years before getting the results! Fortunately, the results given by this method are acceptable as long as the gaussian distribution converges. To check the convergence, we consecutively ran our program with 100, 1000 and 10000 simulations, all converging to the same result.

2.3.2 Tensors and simulations

We used our Hamiltonian determination procedure on two different malonic acid crystals: centrally-labelled and laterally-labelled. The data we have on fully-labelled malonic acid was too complex to be analyzed with this procedure in the first place, but since our the Hamiltonian (equation 2.1) is linear, we can still use all these results to work with fully-labelled malonic acid.

The $\vec{g}$-tensor for malonic acid had already been published [29], as well as the hyperfine tensors of the hydrogen and central carbon [30]. On the contrary, the hyperfine tensor for the lateral carbons is a new result, even if we have been unable to distinguish between those two nuclear spins.

$$\vec{g}^{pub.} = \begin{bmatrix} 2.0023 & & \\ & 2.0033 & \\ & & 2.0037 \end{bmatrix} = 2.0031 \cdot \mathbb{1} + \begin{bmatrix} -8 & & \\ & 2 & \\ & & 6 \end{bmatrix} \cdot 10^{-4}$$

$$\Delta g^{pub.} = 0.00002$$

$$\vec{g}^{exp.} = \begin{bmatrix} 2.0048 & & \\ & 2.0056 & \\ & & 2.0061 \end{bmatrix} = 2.0055 \cdot \mathbb{1} + \begin{bmatrix} -7 & & \\ & 1 & \\ & & 6 \end{bmatrix} \cdot 10^{-4}$$

$$\Delta g^{exp.} = 0.013$$

$$Q_g^{exp.} = \begin{array}{ccc} x & y & z \end{array}$$
$$Q_g^{exp.} = \left[\begin{array}{c|c|c} -0.3620 & 0.8930 & -0.2674 \\ 0.9322 & 0.3472 & -0.1024 \\ 0.0014 & -0.2863 & -0.9581 \end{array}\right] \quad \text{(direction cosines to the hydrogen hyperfine tensor eigenbasis)}$$

$$\vec{A}_H^{pub.} = \begin{bmatrix} 29.3 & & \\ & 58.3 & \\ & & 91.0 \end{bmatrix} \text{ MHz} = 59.3 \cdot \mathbb{1} + \begin{bmatrix} -30 & & \\ & -1 & \\ & & 31.7 \end{bmatrix} \text{ MHz}$$

$$\Delta A_H^{pub.} = 1 \text{ MHz}$$

$$\vec{A}_H^{exp.} = \begin{bmatrix} 31.3 & & \\ & 57.8 & \\ & & 87.6 \end{bmatrix} \text{ MHz} = 58.9 \cdot \mathbb{1} + \begin{bmatrix} -27.6 & & \\ & -1.1 & \\ & & 28.6 \end{bmatrix} \text{ MHz}$$

$$\Delta A_H^{exp.} = 6 \text{ MHz}$$

$$Q_H^{exp.} = \mathbb{1} \text{ (direction cosines to the hydrogen hyperfine tensor eigenbasis)}$$

$$\vec{A}_{C_m}^{pub.} = \begin{bmatrix} 22.8 & & \\ & 42.2 & \\ & & 212.7 \end{bmatrix} \text{MHz} = 92.4 \cdot \mathbb{1} + \begin{bmatrix} -70.2 & & \\ & -50.2 & \\ & & 120.3 \end{bmatrix} \text{MHz}$$

$$\Delta A_{C_m}^{pub.} = \begin{bmatrix} 1.5 & & \\ & 1.0 & \\ & & 0.5 \end{bmatrix} \text{MHz}$$

$$\vec{A}_{C_m}^{exp.} = \begin{bmatrix} 29.5 & & \\ & 44.1 & \\ & & 216.1 \end{bmatrix} \text{MHz} = 96.6 \cdot \mathbb{1} + \begin{bmatrix} -67.1 & & \\ & -52.5 & \\ & & 119.5 \end{bmatrix} \text{MHz}$$

$$\Delta A_{C_m}^{exp.} = 10 \text{ MHz}$$

$$Q_{C_m}^{exp.} = \begin{array}{ccc} x & y & z \end{array}$$
$$Q_{C_m}^{exp.} = \begin{bmatrix} 0.8858 & 0.4607 & 0.0562 \\ -0.0613 & -0.0040 & 0.9981 \\ 0.4601 & -0.8875 & 0.0247 \end{bmatrix} \quad \text{(direction cosines to the hydrogen hyperfine tensor eigenbasis)}$$

$$\vec{A}_{C_{1/2}}^{exp.} = \begin{bmatrix} 36.7 & & \\ & 39.4. & \\ & & 40.3 \end{bmatrix} \text{MHz} = 38.8 \cdot \mathbb{1} + \begin{bmatrix} -2.1 & & \\ & 0.6 & \\ & & 1.5 \end{bmatrix} \text{MHz}$$

$$\Delta A_{C_{1/2}}^{exp.} = 1.3 \text{ MHz}$$

$$\begin{array}{ccc} x & y & z \end{array}$$
$$Q_{C_{1/2}}^{exp.} = \begin{bmatrix} 0.0096 & 0.8667 & 0.4987 \\ -0.1547 & 0.4940 & -0.8556 \\ -0.9879 & -0.0689 & 0.1388 \end{bmatrix} \quad \text{(direction cosines to the hydrogen hyperfine tensor eigenbasis)}$$

In addition, for laterally-labelled malonic acid, we found $\varphi = 94.8°$ and $\psi = 87.5°$, which is very close to what we were expecting as we tried to make the rotation angles

between measured planes as close to 90° as possible. For centrally-labelled malonic acid, we obtained $\varphi = -87.1°$ and $\psi = 81.3°$.

2.3.3 Simulations

Using the direction cosines of the eigenbasis for the proton hyperfine tensor, published by Goedkoop and MacGillavry [24], along with our results, we can identify the orientations of the magnetic field corresponding to our measurements in plane 1, plane 2 and plane 3 with respect to the unit cell of the crystal.
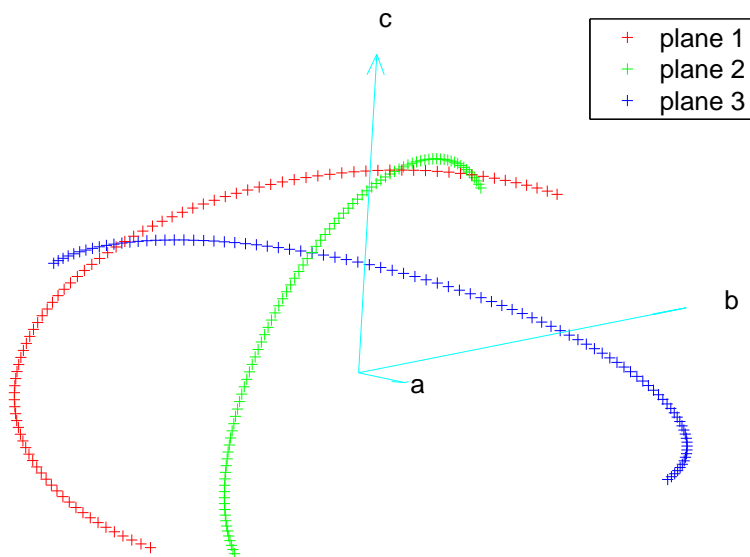
Figure 2.14: Orientation of the magnetic field in the unit cell corresponding to our measurements. The unit cell is denoted by the cyan vectors $\vec{a}$, $\vec{b}$ and $\vec{c}$. The orientation of the magnetic field for the measurements in plane 1, 2 and 3 appear respectively as red, green and blue crosses.
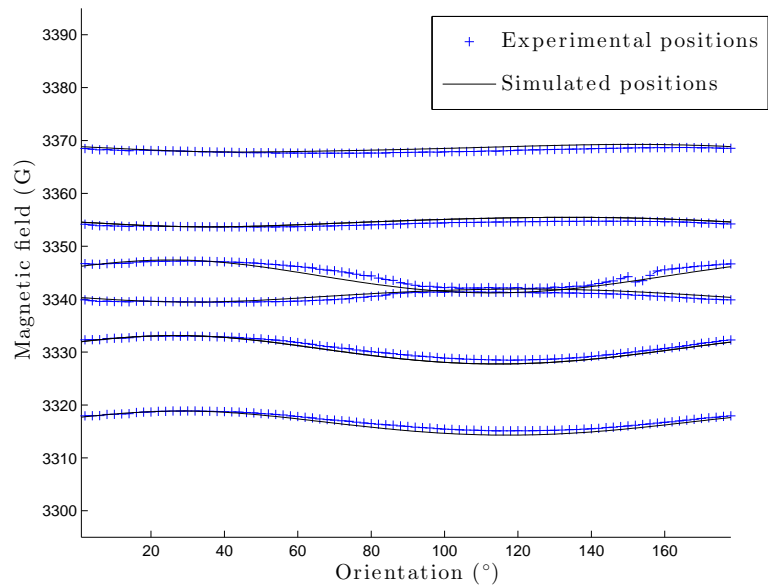
Figure 2.15: Simulation of plane 1 for laterally-labelled malonic acid.
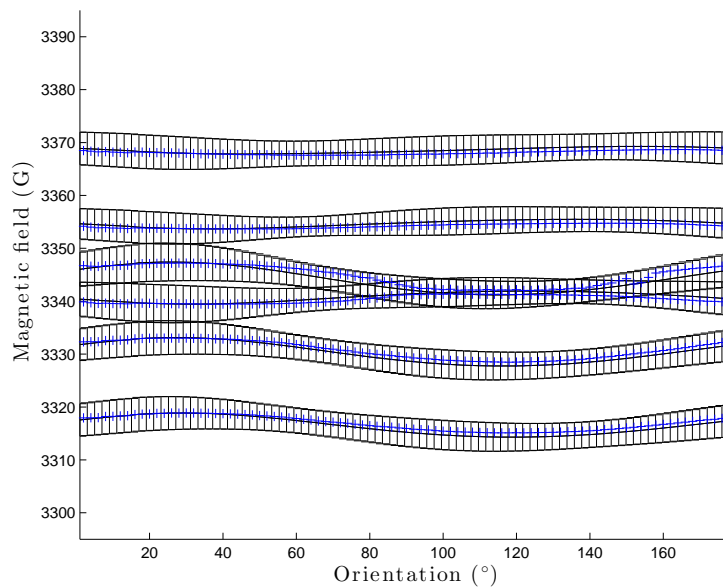
Figure 2.16: Simulation of plane 1 with error bars for laterally-labelled malonic acid .
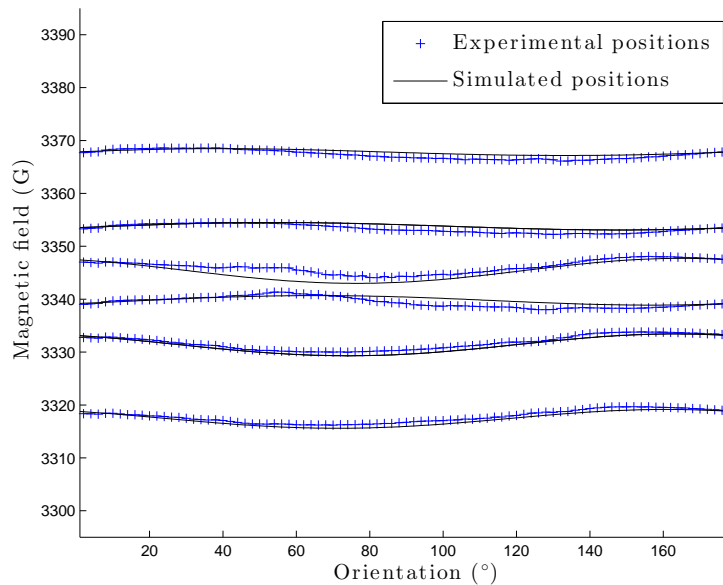
Figure 2.17: Simulation of plane 2 for laterally-labelled malonic acid.
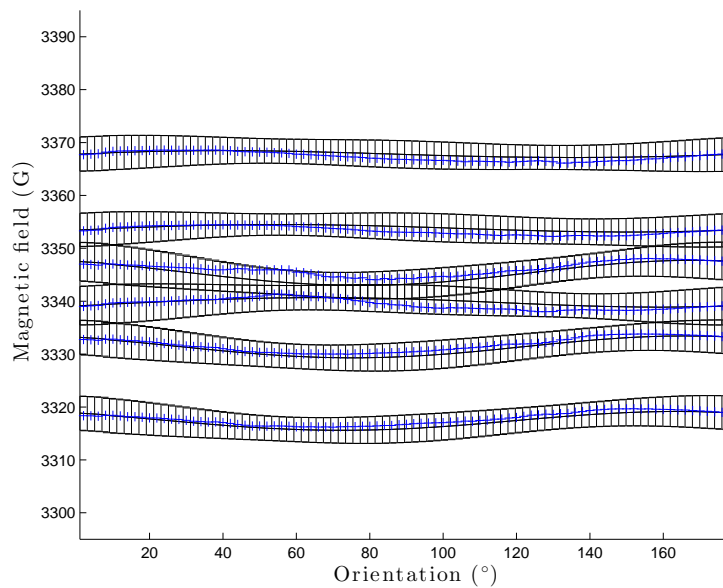
Figure 2.18: Simulation of plane 2 with error bars for laterally-labelled malonic acid.
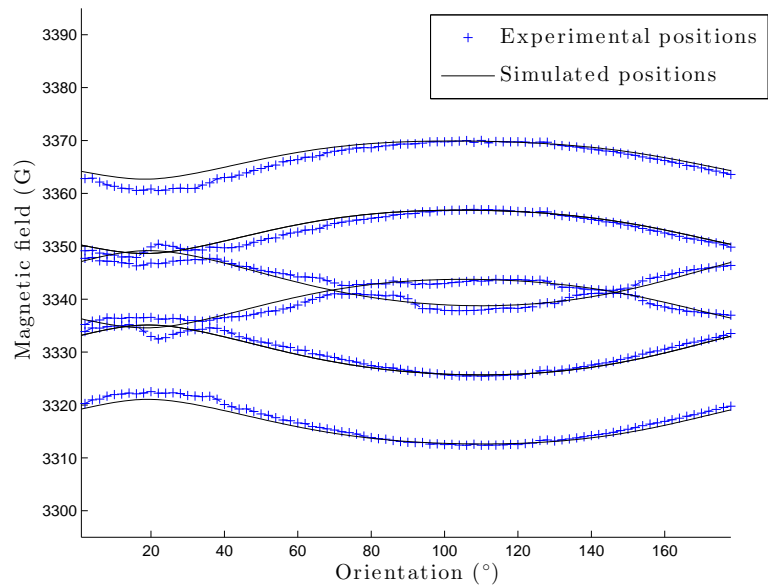
Figure 2.19: Simulation of plane 3 for laterally-labelled malonic acid.
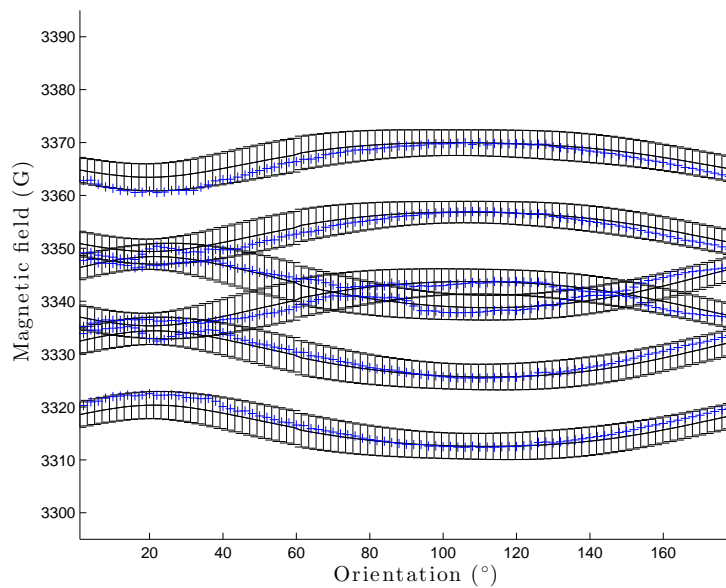
Figure 2.20: Simulation of plane 3 with error bars for laterally-labelled malonic acid .

2.3.4 Conclusion

With the algorithm we designed and implemented, we have a rather quick way to characterize a single crystal sample for ESR experiments. Indeed, measuring ESR spectra in 3 planes with a reasonable angle step (between 2° and 10°) takes a few hours, while most of the algorithm is automated.

What is more is that the simulation algorithm presented in the next chapter allows us to check the relevance of our results very quickly as well. This knowledge of the Hamiltonian will, in the future, allow us to reach the high-fidelity control needed to implement complex algorithms such as algorithmic cooling and quantum error correction.

However, we are still working on refining the uncertainties for our tensors, through a more precise error estimation. Also, for laterally-labelled malonic acid, we plan to use the fact that the overlapping peaks are broader to extract two different tensors for the two lateral carbons. These results will be the topic of a future publication, described in the next section.

2.3.5 Future work using these results

While the Hamiltonian extraction method can be used for different samples, we plan to complete our study of malonic acid with a scientific publication.

First of all, we want to show that we have been able to relax some of the usual assumptions and experimental setups usually necessary to complete this kind of study. Secondly, even if we have not been able to distinguish the peaks coming from the lateral carbons in $1, 3$ ^{13}C malonic acid, the hyperfine tensor we determined for both of them is a new result.

Eventually, while our original goal was to determine the hyperfine tensors for H, C_m, C_1 and C_2 from measurements on fully-labelled malonic acid, the procedure was not successful due to the complex structure of the CW ESR spectra measured (16 peaks and many overlaps). On the other hand, our procedure worked very well for laterally-labelled malonic acid, but also for centrally-labelled malonic acid.

Since the Hamiltonian we consider is linear (see equation 2.1), putting the tensors we measured in different frames and on different molecules in the same basis still allows us to write the Hamiltonian for fully-labelled malonic acid. The final objective of the scientific article we plan to publish soon would then be to show that using this knowledge, we are able to predict and explain the measurements we did on fully-labelled malonic acid. This would be a starting point to further works with this 5-spin system.

Chapter 3

Simulation

In order to predict the results of experiments we plan to run or understand the results of some measurements, we have to be able to simulate these experiments. While I wrote the CW simulator, our pulsed-ESR simulator contains some parts adapted from the pulsed-NMR simulation code written by Dr. Colm Ryan a few years ago. Dr. Ryan later adapted it to ESR and made compatible with our spectrometer: it is for example using the same pulse programs, allowing us to compare very easily simulations with actual experiments. Daniel K. Park and I, to a lesser extent, brought some new features for Electron Nuclear Double Resonance (ENDOR) simulation: we made our code able to simulate pulsed-(ENDOR) experiments, since we also worked on the spectrometer itself to add a radio-frequency (RF) channel.

3.1   Simulation of CW experiments

3.1.1   Pseudo-secular approximation

If we want to express the Hamiltonian of the system in one specific orientation (defined by $\vec{B}_0 = B_0\hat{z}$), we can make the pseudo-secular approximation. The axis system can also be redefined so that we can separate the hyperfine interactions for each nuclear spins species

into two contributions [31]. One is along the external magnetic field and is called *isotropric hyperfine interaction* and is often written as a scalar a. The other one is orthogonal to the field and is called *anisotropic hyperfine interaction*, commonly written b.

This choice leads us to the final form of the Hamiltonian of the system considering our model and its assumptions [31].

$$\hat{H} = \omega_S \hat{S}_Z + \sum_{n=1}^{K} \omega_{I,n} \hat{I}_{n,Z} + \sum_{n=1}^{K} a_n \hat{S}_Z \hat{I}_{n,Z} + \sum_{n=1}^{K} b_n \hat{S}_Z \hat{I}_{n,X} \tag{3.1}$$

$$\text{Where}: a_n = \vec{A}_{n,zz} \text{ and } b_n = \sqrt{\vec{A}^2_{n,zx} + \vec{A}^2_{n,zy}}$$

$$\omega_S = \frac{\vec{g}_{zz} \mu_B}{h} B_0$$

To simulate CW spectra, one has to know that the peaks that appear correspond to transition frequencies. The term transition indicates that under pulse at that particular frequency, the system is brought from one quantum state to another one. Each of those two states corresponds to a unique energy level and the transition frequency is the difference between those two energy levels, expressed in frequency units.

As a consequence, simulating CW spectra implies knowing all the allowed energy levels for the system considered. In quantum mechanics, those energy levels are easily found when the Hamiltonian is known, as they correspond the its eigenvalues (usually referred as eigenenergies).

Considering an chosen orientation of the external magnetic field in the crystal frame, we can determine the coefficients of the interaction tensors and then create the Hamiltonian matrix. The diagonalization matrix for this Hamiltonian can also be created as follows [31]:

$$U = \exp\left[-i \sum_{n=1}^{K} \left(\eta_{\alpha,n} \hat{S}^\alpha \hat{I}_{n,Y} + \eta_{\beta,n} \hat{S}^\beta \hat{I}_{n,Y} \right) \right] \tag{3.2}$$

$$\text{With } \hat{S}^\alpha = \frac{\mathbb{1}}{2} + \hat{S}_Z \text{ and } \hat{S}^\beta = \frac{\mathbb{1}}{2} - \hat{S}_Z$$

$$\eta_{\alpha,n} = \arctan\left(\frac{-b_n}{a_n + 2\omega_{I,n}} \right) \text{ and } \eta_{\beta,n} = \arctan\left(\frac{-b_n}{a_n - 2\omega_{I,n}} \right)$$

Which gives us the diagonal form of our Hamiltonian as follows.

$$\text{And } H_d = U\hat{H}U^\dagger \tag{3.3}$$

$$H_d = \begin{pmatrix} E_1 & & & & & & \\ & \ddots & & & & 0 & \\ & & E_n & & & & \\ & & & \ddots & & & \\ & 0 & & & E_m & & \\ & & & & & \ddots & \\ & & & & & & E_{K+1} \end{pmatrix}$$

As a consequence, H_d is diagonal and its components are the eigenergies of the system. Since the peaks we will see in the CW spectrum are the transitions between certain states, their position is the difference between some eigenenergies that we know: the transition frequency between $|n\rangle$ and $|m\rangle$ is $f_{mn} = |E_m - E_n|$.

For tensor extraction, we only detected and used the allowed transitions peaks. For simulation of real experiments, however, we have to consider all the transitions frequencies present in a certain field strength range, no matter if they are allowed or forbidden.

Once in possession of the transitions frequencies in the desired range of magnetic field strength, we have to determine the amplitude of the peaks. To do that, we can simply compute the coefficients of $\tilde{X} = U\hat{S}_X U^\dagger$. Indeed, the amplitude of the peak for the f_{mn} transition is given by $|\tilde{x}_{mn}|^2$.

3.1.2   Results of CW simulations

Since we know the Hamiltonian of the system quite well, we are able to simulate different kinds of CW spectra in any desired orientation. In addition to the CW ESR spectra presented in the previous chapter, we can for example simulate (and then *predict*) the

frequency of the NMR transitions: the CW ENDOR spectrum. This turned out to be very useful when we worked on implementing algorithmic cooling (cf. Chapter 5) in partnership with Takeji Takui's group in Osaka City University, Japan.

Since simulations of CW ESR transitions peaks trajectories have already been shown in section 2.3, we show here some examples of predictions made using our simulation code.
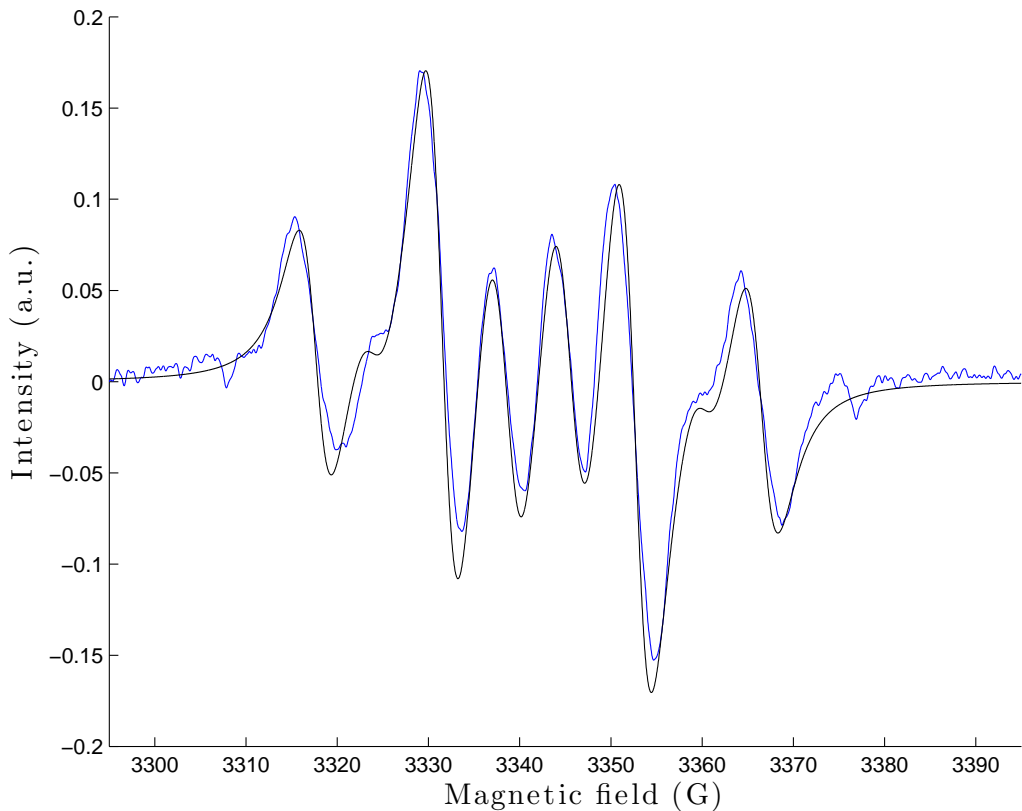
Figure 3.1: Simulation of a CW ESR spectrum for laterally-labelled malonic acid. The chosen orientation of the magnetic field is taken to be the same as in our P2A57 measurement (fifty-eighth measurement in plane 2). The linewidth was taken to be 3.2G (as measured), which corresponds to 18MHz (i.e. $T_2^* \approx 17$ns).
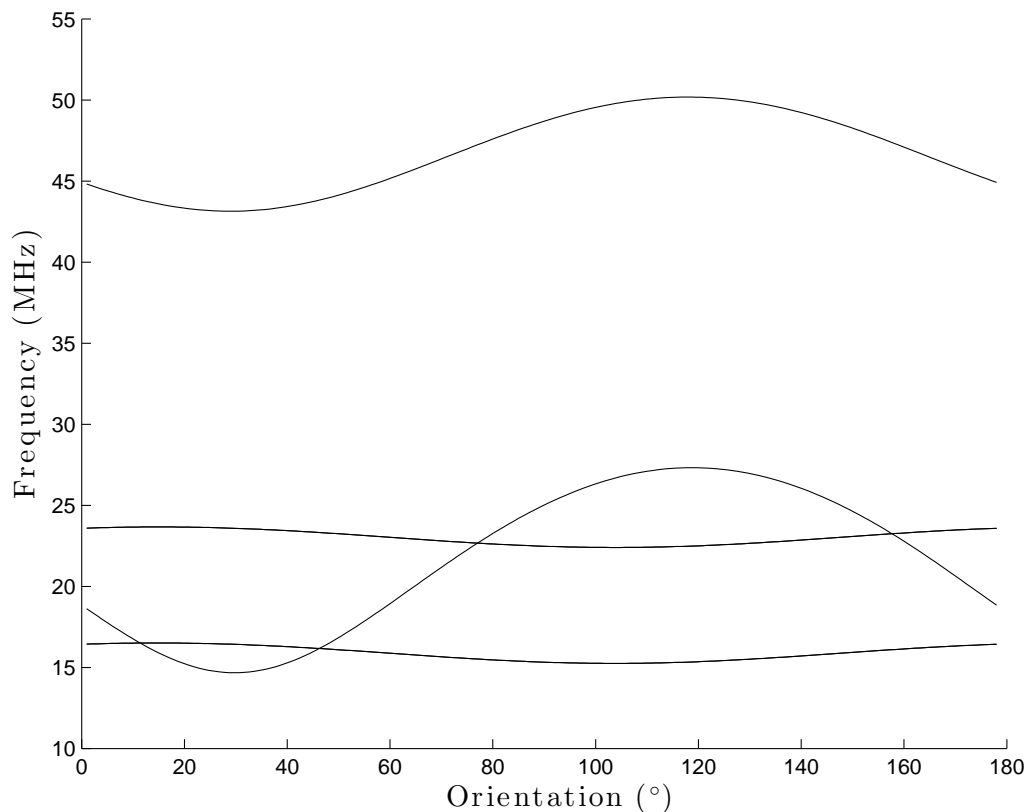
Figure 3.2: Simulation of allowed NMR transition peaks trajectories in plane 1 for our laterally-labelled crystal. Again, because the hyperfine tensors for the two lateral carbons are the same, their NMR transition peaks overlap. Being able to determine the NMR transition frequencies for any orientation of the external magnetic field with respect to our crystal is essential for the optimal orientation procedure shown in section 4.2. Indeed, our pulsed-ESR spectrometer allows us to measure some of these transitions and hence check the orientation the crystal is sitting in corresponds to the optimal one.

3.2 Simulation of pulsed experiments

3.2.1 Simulation of the time evolution

Initial state

Similarly to NMR, the ESR thermal equilibrium state of the system is given, by the Boltzman distribution. $\hat{H}_{int.}$ refers to the internal Hamiltonian given by equation 3.1.

$$\rho_{therm.} = \frac{e^{-\hat{H}_{int.}/k_B T}}{\text{Tr}(e^{-\hat{H}_{int.}/k_B T})} \tag{3.4}$$

We can always make the "high temperature" approximation, i.e. $k_B T \gg |\hat{H}|$. As a consequence, the two first terms of the Taylor expansion are a good approximation of the density matrix of the thermal equilibrium state.

$$\rho_{them.} \approx \frac{1}{2}\left(\mathbb{1} - \frac{\hat{H}_{int.}}{k_B T}\right) \tag{3.5}$$

In that situation, we will prefer to work with the deviation density matrix $\rho_{dev.}$

$$\rho_{dev.} = -\frac{\hat{H}_{int.}}{2k_B T} \tag{3.6}$$

Since we know that the Zeeman energy of the electron is the dominant term in the internal Hamiltonian of the system (by a factor of about 10^3), we can obtain a good approximation of our thermal state.

$$\rho_{dev.} \approx \frac{\hbar\omega_S}{4k_B T}\hat{S}_Z \tag{3.7}$$

Time-dependent Hamiltonian

The Hamiltonian $\hat{H}_{int.}$ given by equation 3.1 is still the internal Hamiltonian of our system. To understand and simulate the behaviour of the system under the pulsed control of our

spectrometer, we have to add the control Hamiltonian, often denoted as $\hat{H}_{RF}$ in NMR conventions. We stuck to this "convention", even if in our case, the control Hamiltonian is in the microwave range.

$$\hat{H}(t) = \hat{H}_{int.} + \hat{H}_{RF}(t) \tag{3.8}$$

The pulse sequence consists of microwave pulses applied in the X-Y plane of the spectrometer. The control we have allows us to change the amplitudes of these pulses on a timescale of a nanosecond.

$$\hat{H}_{RF}(t) = \gamma_e \vec{S} \cdot \vec{B}_1(t) \tag{3.9}$$

$$\tilde{H}_{RF}(t) = \gamma_e \hat{S}_X \tilde{B}_1^X(t) \text{ in the rotating frame.} \tag{3.10}$$

Unitary evolution

This first way to solve the time evolution of the system does not take into account the effects of decoherence. The time evolution of a closed quantum system state is given, in the density matrix formalism, by the Von Neumann equation:

$$\hbar \frac{\partial \rho}{\partial t} = -i \left[\hat{H}(t), \rho \right] \tag{3.11}$$

Making the assumption that our Hamiltonian is time-independent during the small time-steps we defined earlier, we calculate the propagator for this short period of time dt at time t_j as U_j, given as follows:

$$U_j = \exp\left(-\frac{i\hat{H}(t_j)dt}{\hbar} \right) \tag{3.12}$$

Once we have our propagator, we can compute the value of the density matrix of the state from one time-step to the next one:

$$\rho(t_j) = U_j \rho(t_{j-1}) U_j^\dagger \tag{3.13}$$

Lindblad equation and superoperator formalism

If we want to take into account the effects of decoherence in our simulations, we now have to consider an open quantum system. Decoherence is the result of the undesired interactions between the system and the surrounding environment. We consider the environment has no memory, the dynamics of the system follow an equation slightly different from the Von Neumann equation: the Lindblad equation.

$$\hbar \frac{\partial \rho}{\partial t} = -i \left[\hat{H}(t), \rho \right] + \underbrace{\sum_k \left(L_k \rho L_k^\dagger - \frac{1}{2} \left\{ L_k L_k^\dagger, \rho \right\} \right)}_{D(\rho)} \tag{3.14}$$

where: $\begin{cases} \{,\} \text{ denotes the anticommutator} \\ L_k \text{ is the } k^{th} \text{ Lindblad operator} \\ D(\rho) \text{ is called the dissipator} \end{cases}$

We use this formalism to simulate the effect of the relaxation times of the electron over the whole system. It can be shown [32] that the Lindblad operators for the T_1 and T_2 processes are given by :

$$T_1 \Rightarrow L_1 = \sqrt{\frac{p}{T_1}} \hat{S}^\alpha \text{ and } L_2 = \sqrt{\frac{1-p}{T_1}} \hat{S}^\beta \text{ , where } p \approx \frac{1}{2} \left(1 - \frac{\hbar \omega_S}{2 k_B T} \right) \tag{3.15}$$

$$T_2 \Rightarrow L_3 = \sqrt{\frac{1}{2 T_2}} \hat{S}_Z \tag{3.16}$$

To solve the dynamics of the system, we can also use the superoperator formalism. We are then acting on a different space : let $||\hat{\rho}_{therm.}\rangle\rangle$ design the vector made by stacking all the columns of $\rho_{therm.}$. The time evolution of the system is then described by the action of a superoperator $\hat{\Lambda}$ on this vector $||\hat{\rho}_{therm.}\rangle\rangle$.

$$\hat{\Lambda} = e^{-iH+D} \tag{3.17}$$

where : $\begin{cases} H = \hat{H}^* \otimes \mathbb{1} - \mathbb{1} \otimes \hat{H} \\ D = -\sum_k \left[L_k^* \otimes L_k - \frac{1}{2} \mathbb{1} \otimes L_k^\dagger L_k - \frac{1}{2} L_k^T L_k^* \otimes \mathbb{1} \right] \end{cases}$

Free induction decay

No matter which method is used to determine the time evolution of the system, the simulated results, just like the actual experimental results, come from the measurement of the Free Induction Decay. The FID corresponds to a measure of the voltage in the X-Y plane of the spectrometer. We can express it as $s_{\text{FID}} = M_X - iM_Y$, where $M_{X/Y}$ denotes the magnetization measured along X/Y. Whence, if we use the lowering operator $\hat{S}^\beta = \frac{1}{2} - \hat{S}_Z$.

$$s_{\text{FID}}(t) = \text{Tr}\left[\rho(t)\hat{S}^\beta\right] \tag{3.18}$$

In most experiments, like Electron Spin Echo Envelope Modulation (ESEEM), we are more interested in the Fourier spectrum of the FID than in the time-dependent signal itself. For example, in 3-pulse ESEEM, the spectrum of the FID reveals peaks at the NMR transition frequencies of the system.
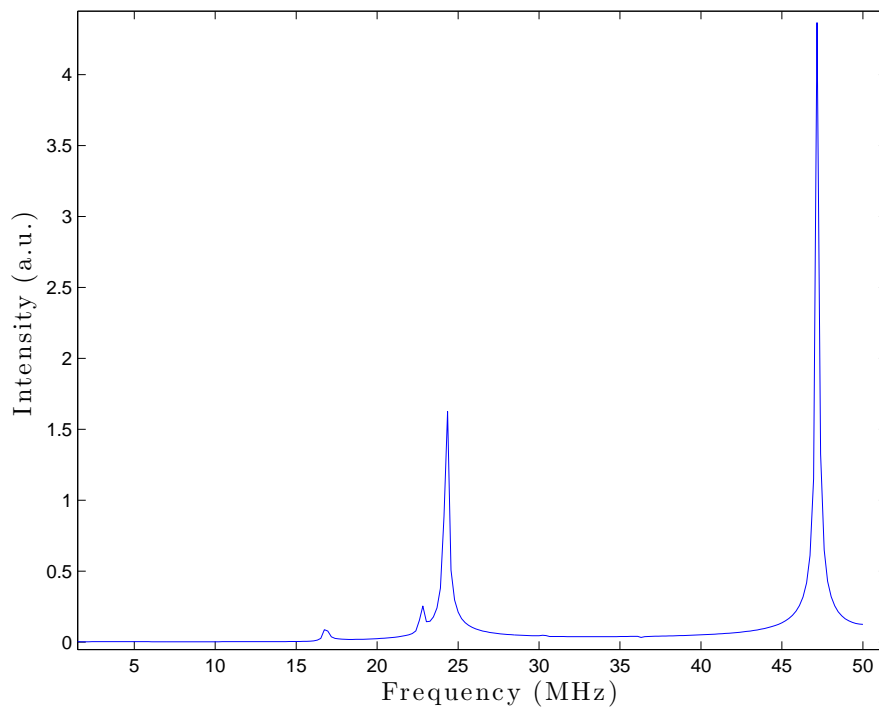
Figure 3.3: Example of 3-pulse Electron Spin Echo Envelope Modulation (ESEEM) Fourier transform simulation for centrally-labelled malonic acid. This simulation, run by Daniel K. Park, takes the following input parameters: $T_1 = 47\mu s$, $T_2 = 6\mu s$, $a_H = 72.671$ MHz, $b_H = 23.764$ MHz, $a_C = -30.44$ MHz and $b_C = 24.672$ MHz. We can see two sets of peaks: the ones with the larger amplitude come from the hydrogen (24 MHz and 47 MHz) while the ones with the smaller amplitude (17 MHz and 23 MHz) come from the central carbon.

Chapter 4

Preparation for experiments

4.1 Overview of pulsed ESR spectrometer

The choice of working with a home-built pulsed-ESR spectrometer [33] rather than with a commercial one stems from the need to have full control over the system to achieve high-fidelity computations, especially when it comes to control via optimal pulse sequences. The fact that some components can be replaced is also an major point. Over the years, the probes have evolved a lot, and resonators more adapted to the current needs have been designed. Also, different amplifiers were tested to choose the one giving the optimal trade-of between amplification and stability. Notice that we set our Rabi frequency to 25MHz, meaning that with the considered amplifier's maximum power (500W), it takes 40ns for the electron spin to perform a 2π rotation.

51
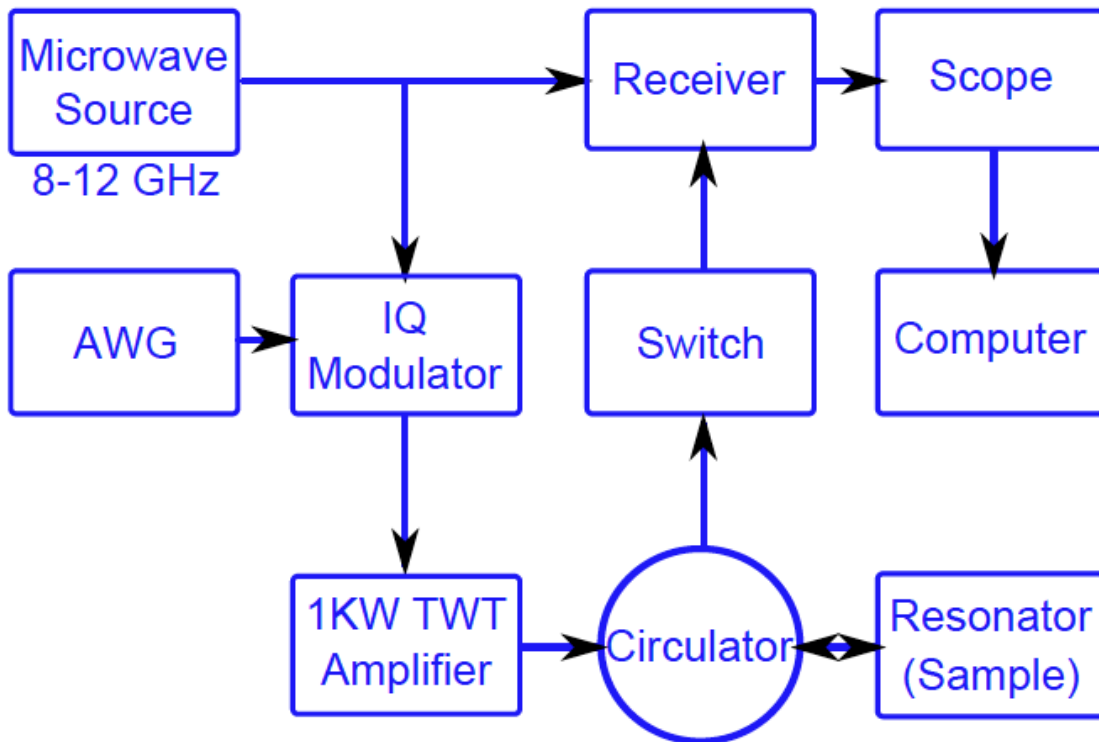
Figure 4.1: Schematic of the homebuilt X-band ESR spectrometer (from [34]). For the input pulses to match the resonance frequency of the resonator, a microwave carrier frequency is provided by the microwave source. The arbitrary waveform generator (AWG) produces the arbitrary pulse shapes. The circulator and the switch ensure the reflected power remains small and does not damage any components nor interfere with the signal coming from the sample. This signal (demodulated or not depending on the oscilloscope that is used) is then displayed on the oscilloscope and also recorded on the computer.

Daniel K. Park designed the current version of our probe. Low-temperature experiments can be run with our spectrometer since the probe can be vacuum-sealed after being inserted in our cryostat. Our spectrometer uses a 2-loop-1-gap copper resonator based on previous designs [34] and an idea by Eaton et al. [35]. The quantum processors that are our malonic acid crystals sit in the small loop. This loop is coupled to the bigger one, which is the one

directly receiving the pulse sequence, through the gap. Daniel K. Park designed 3 similar resonators with slightly different dimensions to adapt to as many samples as possible (the small loop diameter being respectively 1.2mm, 1.6mm and 2mm).
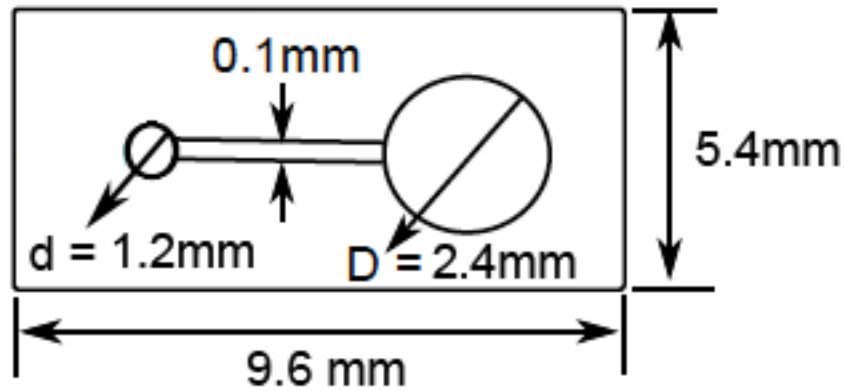
Figure 4.2: Top view of the resonator employed in the pulsed-ESR experiments. The sample is sitting in the smaller loop. The gap can get dirty after being used for a few weeks and needs to be cleaned to prevent dust from making the coupling between the two loops very inefficient in terms of transmitted power.

The main specifications were to have a resonance frequency close to 10GHz and a bandwidth around 200MHz. Two resonators of each of the 3 different designs were ordered from the company ProTechnique EDM in August 2013. In our experiments, considering the sizes of our crystals, we only used the resonator with 1.2mm diameter for the small loop.
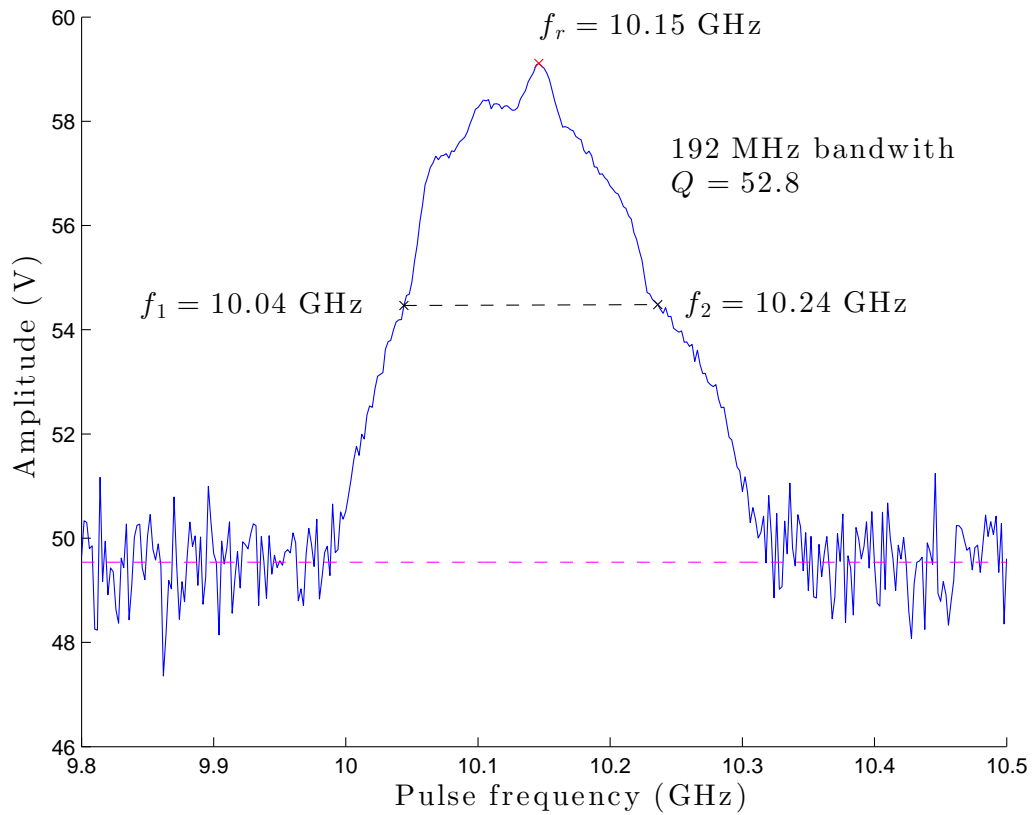
Figure 4.3: Characteristics of the resonator. This measurement was made by Daniel K. Park using the pickup coil and reveals a resonance frequency of 10.15GHz as well as a bandwidth of 192MHz.

A copper box to hold the resonator was designed by Daniel K. Park and machined by me at UW students' machine shop. A cable assembly was made by Roberto J. Romero to guarantee a good coupling between the coaxial cable of the pulsing channel and the larger loop of the resonator. This box is itself held by two lateral bars allowing us to adjust the position of the resonator to maximize the power transmission to the sample as well as the tuning of the resonator. A vector network analyzer belonging to David Cory's group was used during the tuning procedure and allowed us to demonstrate the stability of the tuning from 295K to 4K.

4.2 Crystalline orientation

The whole point of using the electron spin to control the nuclear spins in the system is to avoid having to excite allowed NMR transitions, which take μs, and excite ESR forbidden transitions instead. As said previously, one drawback of exciting forbidden transitions is that the transition rate is much lower than the one for allowed transitions, because instead of rotating just one spin in the system, they rotate two or more at the same time.

To make things more simple (and without loss of generality), let us consider a 1e-1n system. The transition rate for the two allowed transitions can be calculated: $|\cos\eta|$, where $\eta = \frac{1}{2}(\eta_\alpha - \eta_\beta)$. On the other hand, the transition rate for the two forbidden transitions is $|\sin\eta|$. The ESR allowed transitions can be calibrated so that we know that a certain power P is needed for a $\frac{\pi}{2}$-rotation of the electron spin with a $\tau = 10$ns square pulse. The length of a pulse with the same amplitude for the corresponding forbidden transition would then have to be $\frac{\tau}{|\tan\eta|}$ and $\eta \in \left[-\frac{\pi}{4}, \frac{\pi}{4}\right]$ means it takes always more time to excite the forbidden transitions.
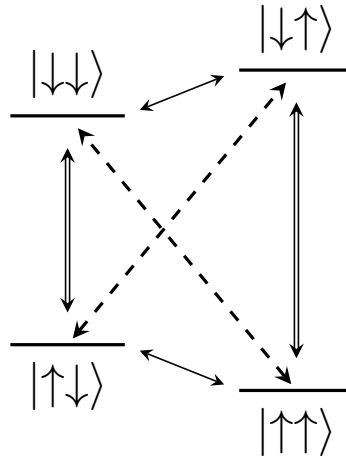

Figure 4.4: Energy diagram for a 1e-1n system given as $|e^-, n\rangle$ showing all the transitions. The allowed ESR transitions are shown as double arrows, NMR allowed transitions as thin arrows and forbidden transitions as dashed arrows.

Still, we can try to put ourselves in the most favourable situation by choosing an orien-

tation of our crystal in which the $|\tan \eta_n|$ of our nuclear spins are large. This orientation can be determined from our knowledge of the Hamiltonian.

4.2.1 Optimization for quantum algorithms

Knowing the Hamiltonian of the system in any desired frame, we chose to work in the eigenbasis of the hyperfine tensor of the hydrogen. The reason for this choice is that the orientation of this eigenbasis in the unit cell of malonic acid crystals has been published in 1972 [36].

Considering the first algorithm we want to implement (detailed in Chapter 5), we worked with one-labelled malonic acid crystals and thus only consider this 1e-2n system, the two nuclear spins being the hydrogen and the central carbon of the molecule. We know that $|\tan \eta_H|$ is usually greater than $|\tan \eta_C|$ and as a consequence, our main concern will be to pick an orientation for which the latter is as large as possible. Yet, we do not want $|\tan \eta_H|$ to be to small either. It turns out that for the maximum value of $|\tan \eta_C|$, $|\tan \eta_H|$ is almost zeros. So we added the constraint that we want $|\tan \eta_H| \geq |\tan \eta_C|$. We finally find an orientation (see figure 4.5), that we call "optimal orientation", in which the two transition rates are comparable: $|\tan \eta_H|^{opt.} = 0.0996$ and $|\tan \eta_C|^{opt.} = 0.0957$.

Knowing the optimal orientation of the magnetic field with respect to our crystal to favour as much as possible the forbidden transitions in our quantum system, our next challenge is to actually orient the crystal as desired with respect to the external magnetic field of our spectrometer.

4.2.2 Crystal cutting and indexing

The crystals we worked on were brought to Dr. Jalil Assoud in his crystallography laboratory. Using big crystals, he would start detecting and cutting obvious parts making the crystal not single. The indexing is then performed using a Bruker X-ray diffractometer. As a result of his measurements, Dr. Assoud sends us a file containing pictures of the crystal under different orientations on which the geometry of the crystal, the unit cell parameters and the Miller indices of the surfaces shown are drawn.

(a) $|\tan\eta_H|$ (b) $|\tan\eta_C|$
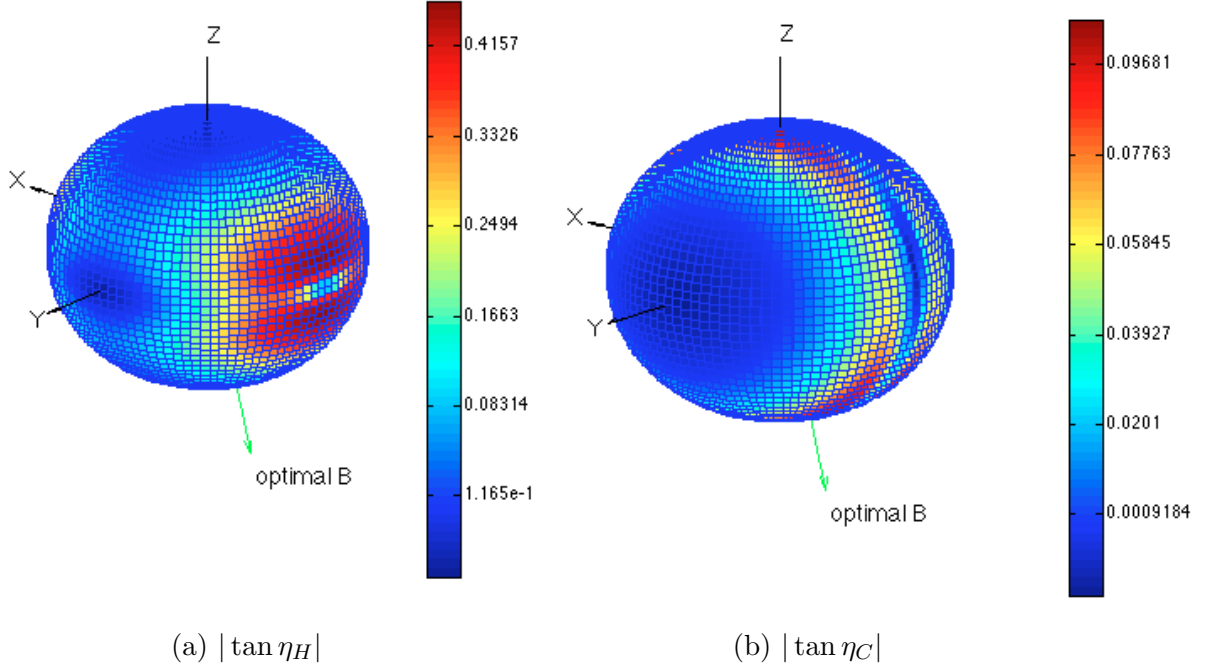
Figure 4.5: Forbidden transition rates for H and C depending on the orientation of the magnetic field in the hydrogen hyperfine tensor principal axis system. We can see that the rate is usually smaller for the carbon, accounting for the fact that we choose our optimal orientation to make it maximum. In this orientation, the two forbidden transition rates are around 0.1.

    The Miller indices allow us to know what surfaces of the crystal are available to help us position the crystal as we want (see Appendix D for more details). One criterion to choose which surface of the crystal to use is the area of said surface: if the area is too small, sticking the crystal on our special holder is going to be very difficult. We also to chose one of the borders of this surface, to be used as a rotation axis in our positioning procedure.
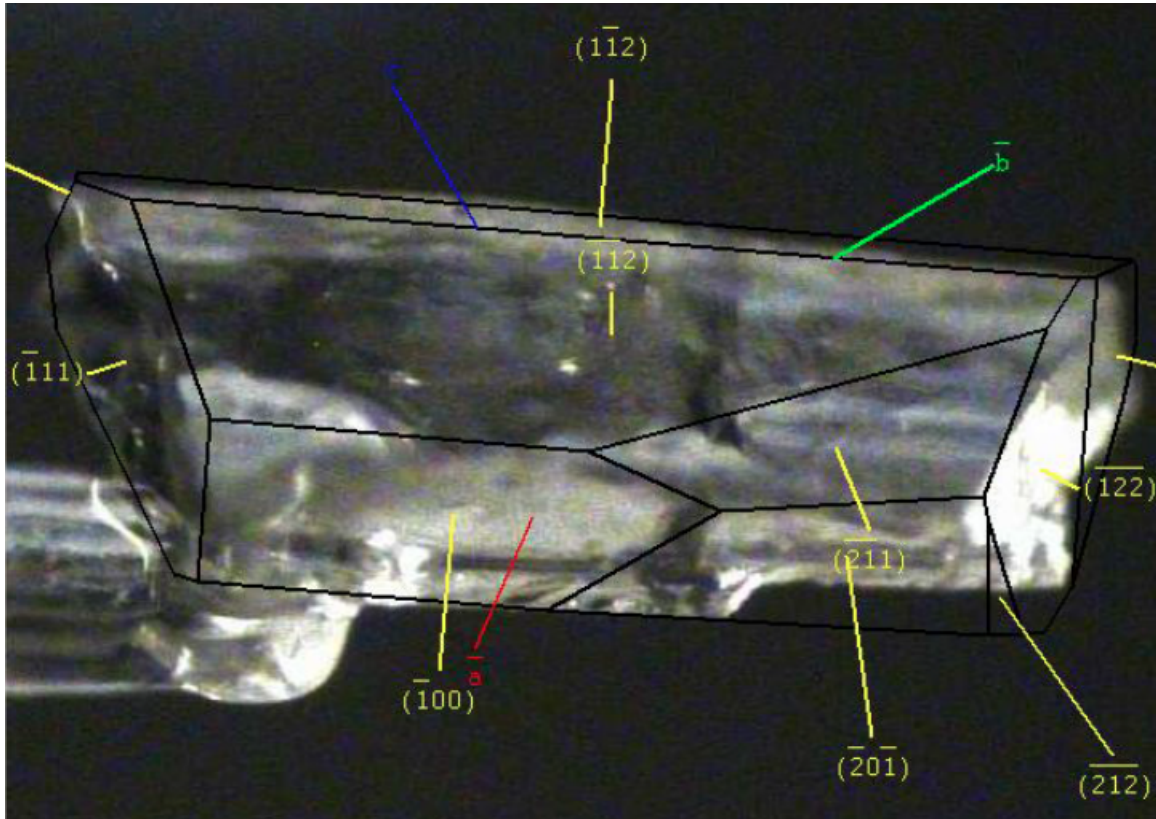
Figure 4.6: Example of indexing results for which we thank Dr. Jalil Assoud. The picture of the crystal in that orientation also contains the black lines outlining the geometry of the crystal. The unit cell parameters are also drawn ($\vec{a}$ in red, $\vec{b}$ in green and $\vec{c}$ in blue). Eventually, yellow lines terminated by Miller indices allow us to understand which surfaces of the crystal we are observing and can use for positioning.

4.2.3   Machining of the sample holder

The crystal has to be inserted in the small loop in the orientation we want. Since we know the surfaces we can use on the crystal thanks to the indexing results, and the optimal orientation of the crystal in the external magnetic field, we can machine a specific sample holder. This small rexolite piece will be used to hold the crystal upside down in the loop. It was designed by Daniel K. Park.
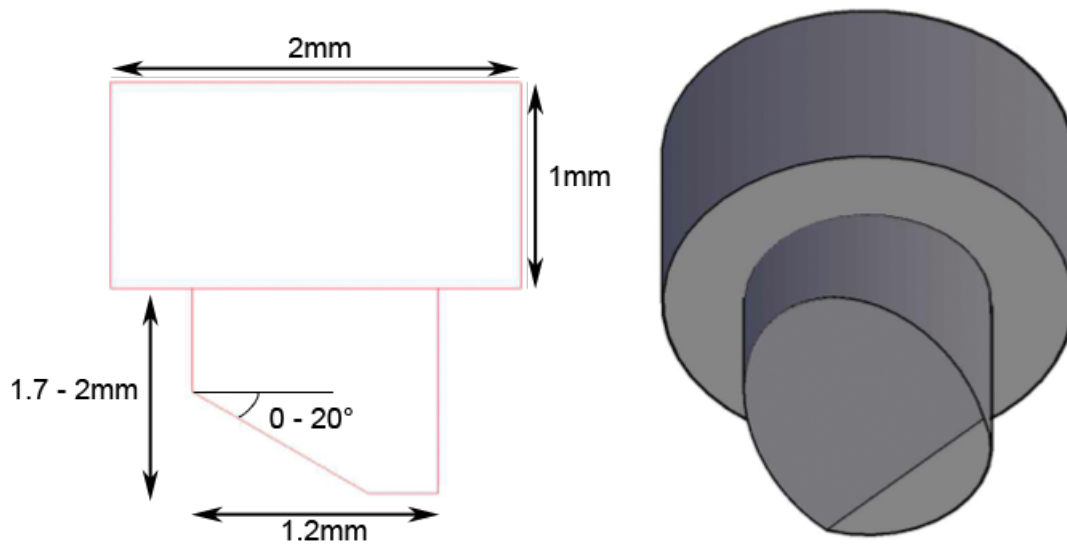
Figure 4.7: Design of the rexolite sample holder. We machined some spare holders for future crystals, with some fixed dimensions (bigger and smaller diameters, for instance). The crystal is stuck on the tilted flat surface, which angle is determined by the choice of the surface of the crystal we decided to use. The flat step is used as a reference to make the positioning successful.

In order to complete this design, we need to choose the surface of the crystal that we want to use. We want this surface to be large enough for reasons explained earlier and we want it to give us a machining angle for the rexolite rod between 0° and 20°. To help us choose among the possible candidates, I wrote a script calculating the angle to cut and the orientation of the optimal orientation with respect to our rod's reference line as functions of the surface we consider to use.
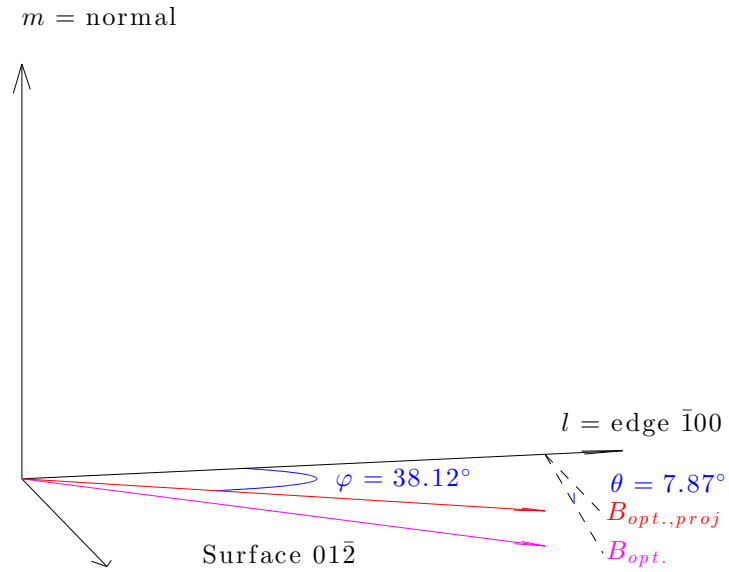
Figure 4.8: Angle to cut and rotation needed for optimal orienting of the crystal when we use the $01\bar{2}$ surface to stick the crystal and the $\bar{1}00$ one for the reference. The final design requires to cut an angle of $8°$ (our precision being $1°$) and rotate our reference line by $38°$ in our magnet.

Following an idea of Hiruy Haile, precision machinist at the students' machine shop of the university, the final procedure to machine the holder includes the machining of a fixture. Its role is to make several steps of the machining of the rod much easier. Holding and machining the fixture instead of the rod directly indeed allows us to works with a bigger, very regular piece instead of the small rod.
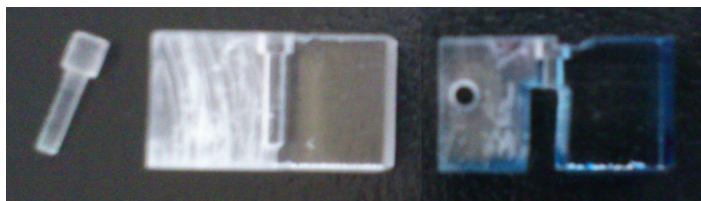
Figure 4.9: Machining of the sample holder. On the left, a rod of rexolite which has not been machined yet. In the middle, a fixture used in the machining procedure. On the right, the same fixture after machining.

4.3 Optimal control with GRAPE pulses

A good knowledge of the Hamiltonian of the crystal in the orientation it is sitting in will allow us to perform optimal control. This is very interesting, especially when the electron spin is used to control the nuclear spins, allowing shorter gates and more complex algorithms [37] [38].

4.3.1 Checking the Hamiltonian

Before actually running experiments with our sample, we have to check that the procedure has been successful and that the crystal is indeed in the right orientation with respect to the external magnetic field.

In order to check the Hamiltonian, we need to measure the ESR spectrum and the ENDOR spectrum. The first one will give us access to the value of g and from the ESR and NMR allowed transitions peaks positions, we will be able to determine a_n and b_n for the nuclear spins in the molecule. Yet, our spectrometer is an ESR spectrometer, and we do not have a direct access to the allowed NMR transitions. Fortunately, 3-pulse Electron Spin Echo Envelope Modulation (ESEEM) allows us to measure the nuclear frequencies of the system indirectly through electron spin echo.

Indeed, if we go back to our example of the 1e-1n system, it can be shown [31] that the two NMR transitions are functions of the a_n and b_n parameters as (defined in equation 3.1)

follows:

$$\omega_{12,n} = \left(\omega_{I,n} + \frac{a_n}{2}\right) \cos\eta_{\alpha,n} - \frac{b_n}{2}\sin\eta_{\alpha,n} \tag{4.1}$$

$$\omega_{34,n} = \left(\omega_{I,n} - \frac{a_n}{2}\right) \cos\eta_{\beta,n} + \frac{b_n}{2}\sin\eta_{\beta,n} \tag{4.2}$$

By choosing the orientation maximizing the forbidden transitions rates, we expect to maximize the amplitude of the ESEEM peaks too. Nevertheless, for some spins, the amplitude of the ESEEM peaks is small compared to the noise level and makes it hard to measure the corresponding a_n and b_n directly. This is actually the other challenge of the crystal orientation procedure. Since we know the Hamiltonian very well and considering small error in the positioning procedure, the crystal should sit in an orientation very close to the optimal orientation we have determined and hence obtain spectra very similar to the predicted ones. If the predicted and measured spectra are close enough, we will be able to claim that we are in the desired orientation, and then, we will know the a_n and b_n coefficients we cannot measure directly from our knowledge of the Hamiltonian.

4.3.2 Pulse-finding and pulse-fixing

GRAPE optimal control

Once the sample is sitting in an orientation for which we know the Hamiltonian well-enough, we can use the GRadient Ascent Pulse Engineering (GRAPE) algorithm to find optimal control pulses [39]. Optimizing on the fidelity of the gate we want to perform with the control pulse ($F = \left|\text{Tr}\left(U_{\text{simulation}}^{\dagger} U_{\text{target}}\right)\right|^2$), the algorithm has two degrees of freedom on for each time step of the pulse: one for the amplitude, the second for its phase.

Our pulse-finding algorithm was written by Dr. Ryan. It allows us to find pulses robust against the Hamiltonian distribution (as the inhomogeneity of the external magnetic field results in some uncertainty on the electron Zeeman splitting) and RF inhomogeneities.

Pulse-fixing and pulse smoothing

Even with a pulse giving a very good fidelity (i.e. $F \geq 0.999$), the hardware is not perfect and there are some non-linearities due to different components and the resonator itself. To make sure the sample actually receives the desired GRAPE pulse, we have a pulse-fixing code, written by Colm Ryan.

One of the challenges in this procedure is that the optimal GRAPE pulse can sometimes have very sudden amplitude changes when the maximum pulse amplitude is reached, which is not physically realizable. To overcome this problem, Daniel K. Park had the idea to add an iteration to the pulse design process. We first find an optimal pulse allowing a maximum amplitude around 10% lower than the amplitude allowing us to do the 10ns 90° rotation. We fix this pulse with Dr Ryan's program. We use the result of the pulse fixing as an initial guess to find an optimal GRAPE pulse, this time allowing a maximum power to perform a 10ns 90° rotation. This pulse is expected to be smooth and not saturate, which is the case in practise.

4.3.3   Benchmarking the control

Once the crystal orientation and Hamiltonian checking procedures are complete, we will be able to characterize the goodness of the control on the system. To do this, we plan to use randomized benchmarking of quantum gates [40].

4.4   Results of the experimental preparation

At the time this thesis is being written, the work on the spectrometer is focusing on the best amplifier to use, looking for a trade-of between linear region size and possible amplification.

As for the crystal positioning with respect to the magnetic field, the procedure has been tried twice, allowing us to learn a lot about each step and getting close to a successful outcome. In those preparatory stages, we worked with unlabelled malonic acid crystals. Among the different difficulties we had to go through, the machining of the rod and the

size of the crystal have been overcome. Indeed, if the crystal is too small, it is really hard to get a good signal from it (a lot of scans have to be ran in order to average the noise out, making the measurements last for hours).

Another problem we had to solve is sticking the crystal on the rod. We first used vaseline, which turned out not to be solid enough: the crystal was really likely to move when the rod was inserted in the resonator's loop. Our second test was ran with Stycast 1266. We discovered that the Stycast did not cure because the air was too humid. Hence for the future works, we know the rod has to be put in a dry container for the Stycast to cure. Moreover, it turns out that cutting the crystal is no longer necessary beforehand. Indeed, after 2 days in the dry container, the parts of the crystal sticking out of the rod diameter (hence not fitting in the loop) can be removed simply by using a q-tip and pure ethanol, while it was really hard to do if the crystal has been exposed to humidity for a few days.

Some crystals are currently being indexed for us to try the most updated version of this orientation procedure, and we are confident we will manage to orient a crystal in the best possible way to favour the forbidden transitions rate and allow fast control of the nuclear spins via the electron spin.
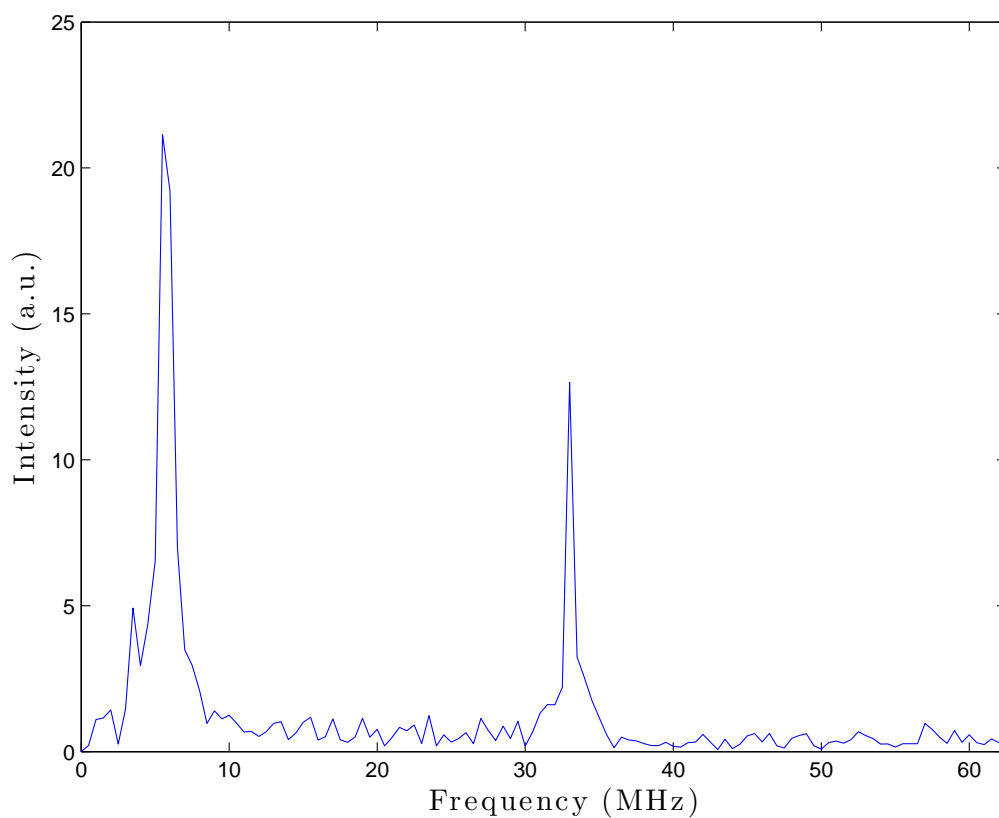
Figure 4.10: Example of 3-pulse Electron Spin Echo Envelope Modulation (ESEEM) Fourier transform for unlabelled malonic acid. This spectrum, measured by Daniel K. Park, shows the two NMR transitions for the hydrogen: one close to 5.5MHz, the other around 33MHz. Thanks to this measurement (along with a measurement of the ESR allowed transitions), we can recover the a_n and b_n parameters of the hydrogen for the orientation we are sitting in and check they correspond to the desired optimal orientation.

Chapter 5

Heat-bath algorithmic cooling

In an ideal world, when we turn on our electromagnet, all our individual spins (as opposed to the ensemble spins we are always talking about in ESR and NMR) would align with the field and all be in the $|0\rangle$ state, resulting in perfect ensemble $|0\rangle$ spin states. Unfortunately, the ensemble of spins follows a Gibbs distribution when it comes to occupying the two eigenenergy levels E_0 and E_1.

Since one of the requirements to engineer a quantum computer is the ability to initialize the qubits in an easily identifiable state like $|00...0\rangle$, we would like to find a way to force as much spins with energy E_1 as possible to move to the E_0 energy level. There are various techniques to setup an experiment and favour the E_0 energy level to get closer to this DiVicenzo criterion, but most of them are technology dependent. Amazingly, there are technology independent methods, and heat-bath algorithmic cooling is one of them.

Implementing algorithmic cooling will help us dynamically provide highly-polarized ancilla qubits to implement quantum error-correcting codes, but interestingly, it is also an algorithm of interest for other purposes. For instance, while usual magnetic resonance imaging techniques rely on proton magnetic resonance spectroscopy, only allowing static analysis, following dynamic processes would require the detection of ^{13}C. Algorithmic cooling would here be used to improve the signal to noise ratio of the carbon-based technique, known to be much worse than for proton-based spectroscopy [41].

5.1 Quantum circuit of the algorithm

Knowing the energy distribution on the two eigenstates, we can define the *polarization* of an ensemble spin as the difference in populations on the state $|0\rangle$ and on the state $|1\rangle$. It can easily be shown that this polarization $\tilde{\epsilon}$ can be expressed as a function of the experimental setup as follows [42]:

$$\tilde{\epsilon} = \tanh \frac{E_1 - E_0}{2 k_B T} \tag{5.1}$$

Heat-bath algorithmic cooling is a method used to boost the polarization on one of the spins in the system. The idea is that a heat-bath of spins pumps the entropy out of the other spins in the system. Eventually, the polarization on those spins can be compressed onto only one spin, resulting in one highly-polarized spin. For instance, with centrally-labelled malonic acid, which is a 3-qubit system, multiple rounds of algorithmic cooling starting from a low polarization $\tilde{\epsilon}_{\text{initial}}$ can, in theory, result in $\tilde{\epsilon}_{\text{final}} = 2\tilde{\epsilon}_{\text{initial}}$.

Heat-bath algorithmic cooling has already been successfully implemented in solid-state NMR [43]. In our case, the electron spin is used both as a heat-bath (its relaxation time being around a thousand times shorter than the nuclear spins') and as the spin which polarization is eventually boosted. We worked in partnership with Takeji Takui's group in Osaka City University in Japan to implement algorithmic cooling with one-labeled malonic acid single crystals.

5.2 Various implementation methods

For our 3-qubit system, the general quantum circuit is shown in figure 5.1. We have 3 different ways to implement this algorithm. Among those, we chose to focus on two methods, corresponding to the machines and knowledge that the two collaborating groups have.

The gates of the algorithm can be decomposed so that only allowed ESR and NMR transition have to be driven (CNOT and Toffoli gates shown in figure 5.2), making the
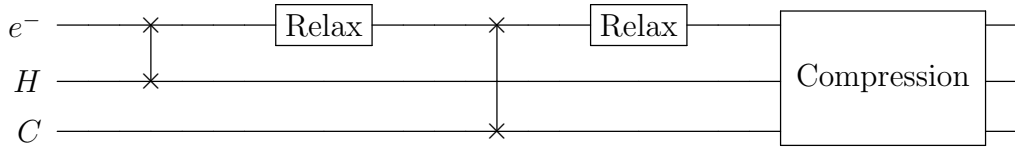
Figure 5.1: Quantum circuit for algorithmic cooling where the electron spin is used as a heat-bath for its fast relaxation time (about 10^3 the one of the nuclear spins). The electron spin is initially the most polarized (about 10^3 more than the nuclear spins). The algorithm starts with two swap gates between the electron and one of the nuclear spins followed by a relaxation time. The relaxation time (around $5T_1^e$) lets the electron spin refresh and recover its thermal polarization $\tilde{\epsilon}$ while the swap gates store the high polarization on the nuclear "memory" qubits. The compression gate consists of a simultaneous flip of the 3 spins in the system.

sequence much shorter. However, this requires a pulsed-ENDOR spectrometer that we do not have yet at IQC. Takeji Takui's group has one and this is why we are working towards implementing algorithmic cooling this way in their laboratory.
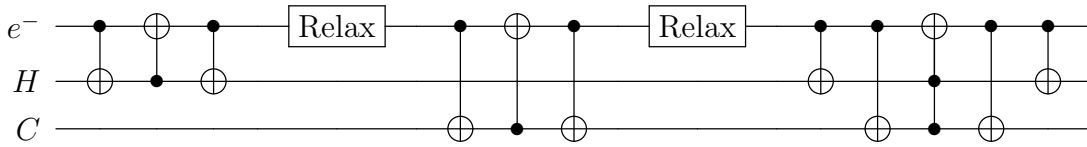
Figure 5.2: Quantum circuit for algorithmic cooling after decomposition of the gates.

The desired gates can also be implemented using square microwave pulses on ESR forbidden transitions frequencies. Indeed, the swap gates flip two spins at a time, while the compression gate flips all three spins in the system. This is hard because the transition rate for such transitions is really low and requires either high-energy (often impossible to reach due to hardware) or pulses so long that they exceed the coherence times of the spins. Our simulations showed us that with the power available in our spectrometer, this method would not boost the polarization of the electron spin.

Since our spectrometer is not able yet to handle RF pulses yet and that pulsing directly

on forbidden transition makes the method irrelevant at our spectrometer power level, we decided to work on implementing the algorithm with optimal control. Using GRAPE pulses, we can get a pulse sequence with "short" pulses (about 200ns) at microwave frequencies only, simply because GRAPE pulses are optimal as opposed to square pulses.

5.3   Results

Takeji Takui's group in Osaka City University (Japan), works with a CW ENDOR and a pulsed-ENDOR spectrometers in which the way the sample is held allows the use of a goniometer and no change of orientation when going from one machine to the other. As a consequence, they started by determining the Hamiltonian of their crystal. Once in the pulsed-ENDOR spectrometer, they could check the orientation was still the same with techniques described before (except they could measure the NMR transitions directly instead of using 3-pulse ESEEM).

When we started the collaboration a few months ago, however, the measurement of the NMR transitions was really noisy and did not allow us to check the Hamiltonian we had was the correct one. The collaboration period happened to be a few weeks before Takeji Takui's machines had to be moved to a different building. Considering the time needed to move those machine safely, this collaboration has not been successful yet.

Chapter 6

Quantum error correction

Quantum error-correcting codes aim at protecting a state from an error likely to happen in a quantum channel or during the implementation of a quantum circuit.

6.1 Concepts and examples

We can imagine a simple situation in which we need to send a qubit $|\psi\rangle = \alpha|0\rangle + \beta|1\rangle$ through a quantum channel. Ideally, the state would not be modified by traveling through the channel:

$$|\psi\rangle \text{———————} |\psi\rangle$$

Experimentally, though, an error E can occur and modify the state. We could then model our error by an undesired quantum gate that is likely to (but might not) act on the state while it travels through the channel.

$$|\psi\rangle \text{——}\boxed{E}\text{——} |\phi\rangle \neq |\psi\rangle$$

The general procedure to design an error-robust quantum circuit in order to protect a state starts with the necessity to identify said error. Then, the input state, to which we

have added a certain number of ancilla qubits, is encoded. This operation will be denoted by a C matrix. Each qubit (the one we want to protect as well as the ancilla qubits) is then randomly impacted or not by an error. The state is then decoded (C^{-1} is applied). Eventually, a recovery gate is applied, leaving us with our successfully protected state and the *syndrome* of the error, carried by the former ancilla qubits.
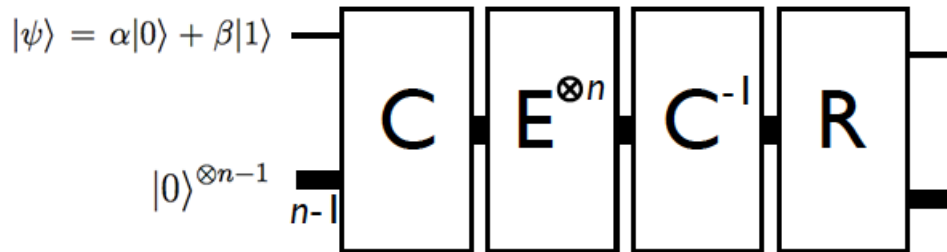

Figure 6.1: The general circuit for quantum error correction (adapted from [44]).

As we work with qubits, all reversible operations can be written in terms of identity and the Pauli matrices. As a practical example, let us then start by correcting X and Z errors, first separately and then with the same circuit.

6.1.1 X or Z error corrections

First, imagine that the error can only be an X operation (bit flip) on the state. To protect $|\psi\rangle$ against this error, we need to add ancilla qubits and send them all through the channel. The ancilla qubits will shield $|\psi\rangle$ and can even give us information on the errors that occurred in the channel.

To do that, we will encode our initial state $|\psi\rangle \otimes |0\rangle \otimes |0\rangle = \alpha|000\rangle + \beta|100\rangle$ before sending it through the channel and eventually decode it once it has got out of it. The quantum error correction circuit would be the following one :

71
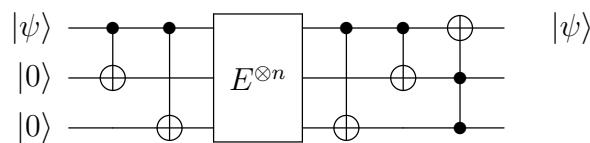
Again, in this situation, the error gate can be III or XII or IXI or even IIX. In all these cases, we would have successfully transferred the state $|\psi\rangle$ from one end of the channel to the other. Also, noticing $Z = H \cdot X$ where H is the well-known Hadamard gate, we can simply adapt our encoding and decoding circuits a little bit to make it correct a Z error.
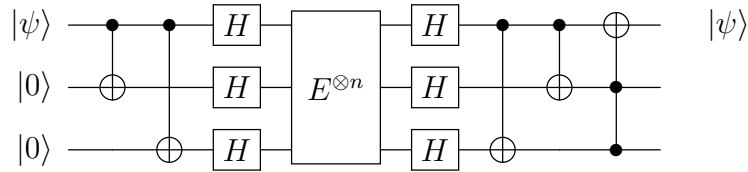
6.1.2 Shor's 9 qubits quantum error-correcting code

The two following examples are interesting and efficient but only in the case when one pre-determined error can occur inside the channel. Let us now consider that any of X and Z errors can occur when traveling through the quantum channel. Obviously, we will need more ancilla qubits to "absorb" these potential errors. The following circuit would work for the two possibilities.
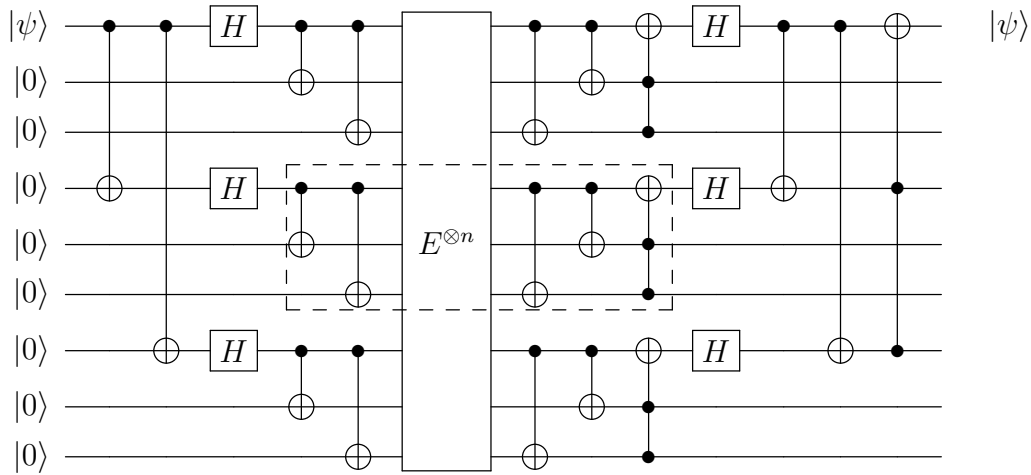
In that circuit, we can recognized the central part (boxed off) takes care of the X errors while the outer part of the circuit deals with Z errors. Moreover, as $Y = iXZ$, this circuit

also corrects Y errors.

6.2 Towards multi-round quantum error correction

One of the constraints of the model presented above is that it requires pure ancilla qubits, which is very hard to prepare in ESR. Apart from the number of ancilla qubits to use, we have to overcome a polarization issue. Yet, it was proved [44] that quantum error correcting codes can be implemented with mixed ancilla qubits by performing the inverse of the recovery operator before the encoding step.
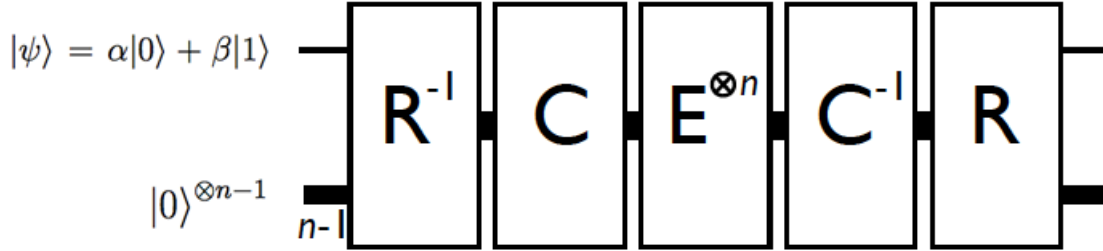
Figure 6.2: The augmented circuit for quantum error correction (adapted from [44]).

The error is corrected as long as the polarization of the ancilla qubits is such that $\tilde{\epsilon}_{\text{anc.}} \geq \sqrt{(2)} - 1 \approx 0.41$, which can be achieved by multiple rounds of heat bath algorithmic cooling. As a comparison, for an electron spin at $T = 1.9$K and a magnetic field of 0.39T (≈ 10.8GHz), $\tilde{\epsilon}_e \approx 0.04$.

With our 1-to-5-qubit samples, we can of course not implement Shor's 9 qubit quantum error-correcting code but we could make a proof of principle. We are still investigating to find and synthesize a sample that would offer more qubits and stable free radicals after irradiation.

Chapter 7

Conclusion

Harnessing the quantum laws of physics to work out computation exponentially faster than classical computers is a beautiful challenge. The work presented in this thesis is a small step forward in the long path to a world with quantum computers.

Starting from incomplete information on our sample, we have been able to set up our own experimental characterization procedure and make it systematic to study different samples. We relaxed the need for a goniometer in the usual CW orientation study of a sample and showed we could still determine the Hamiltonian of our sample precisely enough to predict more complex experiments, using our simulation codes. Those simulation codes were really useful to us in our goal to implement algorithmic cooling and quantum error-correcting codes.

On our way to implementing heat-bath algorithmic cooling, we improved our control on our home-built pulsed-ESR spectrometer and the positioning procedure for our crystals which we expect to be successful soon. From that point on, there are a lot of interesting things to be done and challenging experimental results to obtain.

Of course, there is still work in order to be able to implement quantum algorithms using electron and nuclear spins in single crystals, but we are on the right path to make a proof of principle with our sample and are looking for samples offering more qubits as well as stable radicals on which to apply the knowledge we have accumulated.

APPENDICES

Appendix A

Standardization of unit cell parameters

Since many publications used the unit cell parameters as published in 1957 [24], it is important for us to make sure we understand how these first results are related to the latest refined ones. In order to compare the published values, we have to choose a standard, and we will stick to the choice made by Jagannathan et al. in 1994 [25] to have $\|a\| \leq \|b\| \leq \|c\|$. Table A.1 gives the parameters as they were published in 1957 [24] as well as the standardized version. this appendix details the mathematical transformation from one to the other.

The standardization of these results requires a swap between a and b, also implying the new angles $\alpha' = \pi - \beta$ and $\beta' = \pi - \alpha$.

First, let us explain how to express the unit cell vectors in an orthonormal basis. Since we are only interested in the directions in which $\vec{a}$, $\vec{b}$ and $\vec{c}$ will point to, we can work with the unit vectors $\bar{a}$, $\bar{b}$ and $\bar{c}$. To make things simple, we can choose $\hat{y}$ to be aligned with $\vec{b}$ and $\hat{z}$ to be directly orthogonal to $\hat{y}$ in the plane formed by $\vec{b}$ and $\vec{c}$.

Table A.1: Malonic acid unit cell as published in 1957 and standardization.

Goedkoop and MacGillavry [24]					Standardization			
a	5.33 Å	α	102.7°		a	5.14 Å	α	44.8°
b	5.14 Å	β	135.2°		b	5.33 Å	β	77.3°
c	11.25 Å	γ	85.2°		c	11.25 Å	γ	85.2°

$$\text{Let } \bar{a} = \begin{bmatrix} \bar{a}_x \\ \bar{a}_y \\ \bar{a}_z \end{bmatrix}, \ \bar{b} = Y = \begin{bmatrix} 0 \\ 1 \\ 0 \end{bmatrix}, \ \bar{c} = \begin{bmatrix} 0 \\ \bar{c}_y \\ \bar{c}_z \end{bmatrix}$$

$$\bar{c} \cdot \bar{b} \triangleq \cos \alpha = \bar{c}_y$$

$$\Rightarrow \bar{c} = \begin{bmatrix} 0 \\ \cos \alpha \\ \sin \alpha \end{bmatrix} \quad \text{since } \|\bar{c}\|^2 = 1$$

$$\bar{a} \cdot \bar{b} \triangleq \cos \gamma = \bar{a}_y$$

$$\bar{a} \cdot \bar{c} \triangleq \cos \beta = \bar{a}_y \cos \alpha + \bar{a}_z \sin \alpha$$

$$\Rightarrow \cos \beta = \cos \gamma \cos \alpha + \bar{a}_z \sin \alpha$$

$$\Rightarrow \bar{a}_z = \frac{\cos \beta - \cos \gamma \cos \alpha}{\sin \alpha}$$

$$\bar{a}_x^2 + \bar{a}_y^2 + \bar{a}_z^2 \triangleq 1 \Rightarrow \bar{a}_x = \sqrt{1 - \cos^2 \gamma - \left(\frac{\cos \beta - \cos \gamma \cos \alpha}{\sin \alpha} \right)^2}$$

$$\Rightarrow \bar{a} = \begin{bmatrix} \sqrt{\sin^2 \gamma - \left(\frac{\cos \beta - \cos \gamma \cos \alpha}{\sin \alpha} \right)^2} \\ \cos \gamma \\ \frac{\cos \beta - \cos \gamma \cos \alpha}{\sin \alpha} \end{bmatrix} \quad \text{since } 1 - \cos^2 \gamma = \sin^2 \gamma$$

Hence the transformation relating $(\bar{a}, \bar{b}, \bar{c})$ to a (X, Y, Z) basis :

$$\begin{bmatrix} \sqrt{\sin^2 \gamma - \left(\frac{\cos \beta - \cos \gamma \cos \alpha}{\sin \alpha}\right)^2} & 0 & 0 \\ \cos \gamma & 1 & \cos \alpha \\ \frac{\cos \beta - \cos \gamma \cos \alpha}{\sin \alpha} & 0 & \sin \alpha \end{bmatrix} = \begin{bmatrix} 0.7012 & 0 & 0 \\ 0.0843 & 1 & -0.2198 \\ -0.7080 & 0 & 0.9755 \end{bmatrix}$$

Now let us see how we have to redefine the unit cell so that $(\vec{a}, \vec{b}, \vec{c})$ remains a direct system describing the same crystalline periodicity. To stay in the same frame as before, we will align a (formerly b) in the Y direction.

$$\text{Let } \bar{a} = Y = \begin{bmatrix} 0 \\ 1 \\ 0 \end{bmatrix}, \bar{b} = \begin{bmatrix} \bar{b}_x \\ \bar{b}_y \\ \bar{b}_z \end{bmatrix}, \bar{c} = \begin{bmatrix} 0 \\ \bar{c}_y \\ \bar{c}_z \end{bmatrix}$$

$$\bar{c} \cdot \bar{a} \triangleq \cos \beta = \bar{c}_y$$

$$\Rightarrow \bar{c} = \begin{bmatrix} 0 \\ \cos \beta \\ \sin \beta \end{bmatrix} \text{ since } \|\bar{c}\|^2 = 1$$

78

$$\bar{b} \cdot \bar{a} \triangleq \cos\gamma = \bar{b}_y$$

$$\bar{b} \cdot \bar{c} \triangleq \cos\alpha = \bar{b}_y \cos\beta + \bar{b}_z \sin\beta$$

$$\Rightarrow \cos\alpha = \cos\gamma \cos\beta + \bar{b}_z \sin\beta$$

$$\Rightarrow \bar{b}_z = \frac{\cos\alpha - \cos\gamma \cos\beta}{\sin\beta}$$

$$\bar{b}_x^2 + \bar{b}_y^2 + \bar{b}_z^2 \triangleq 1 \Rightarrow \bar{b}_x = \sqrt{1 - \cos^2\gamma - \left(\frac{\cos\alpha - \cos\gamma \cos\beta}{\sin\beta}\right)^2}$$

$$\Rightarrow \bar{b} = \begin{bmatrix} \sqrt{\sin^2\gamma - \left(\frac{\cos\alpha - \cos\gamma \cos\beta}{\sin\beta}\right)^2} \\ \cos\gamma \\ \frac{\cos\alpha - \cos\gamma \cos\beta}{\sin\beta} \end{bmatrix} \quad \text{since } 1 - \cos^2\gamma = \sin^2\gamma$$

Hence the transformation relating $(\bar{a}, \bar{b}, \bar{c})$ to a (X, Y, Z) basis :

$$\begin{bmatrix} 0 & \sqrt{\sin^2\gamma - \left(\frac{\cos\alpha - \cos\gamma \cos\beta}{\sin\beta}\right)^2} & 0 \\ 1 & \cos\gamma & \cos\beta \\ 0 & \frac{\cos\alpha - \cos\gamma \cos\beta}{\sin\beta} & \sin\beta \end{bmatrix} = \begin{bmatrix} 0 & 0.7012 & 0 \\ 1 & 0.0843 & -0.2198 \\ 0 & -0.7080 & 0.9755 \end{bmatrix}$$
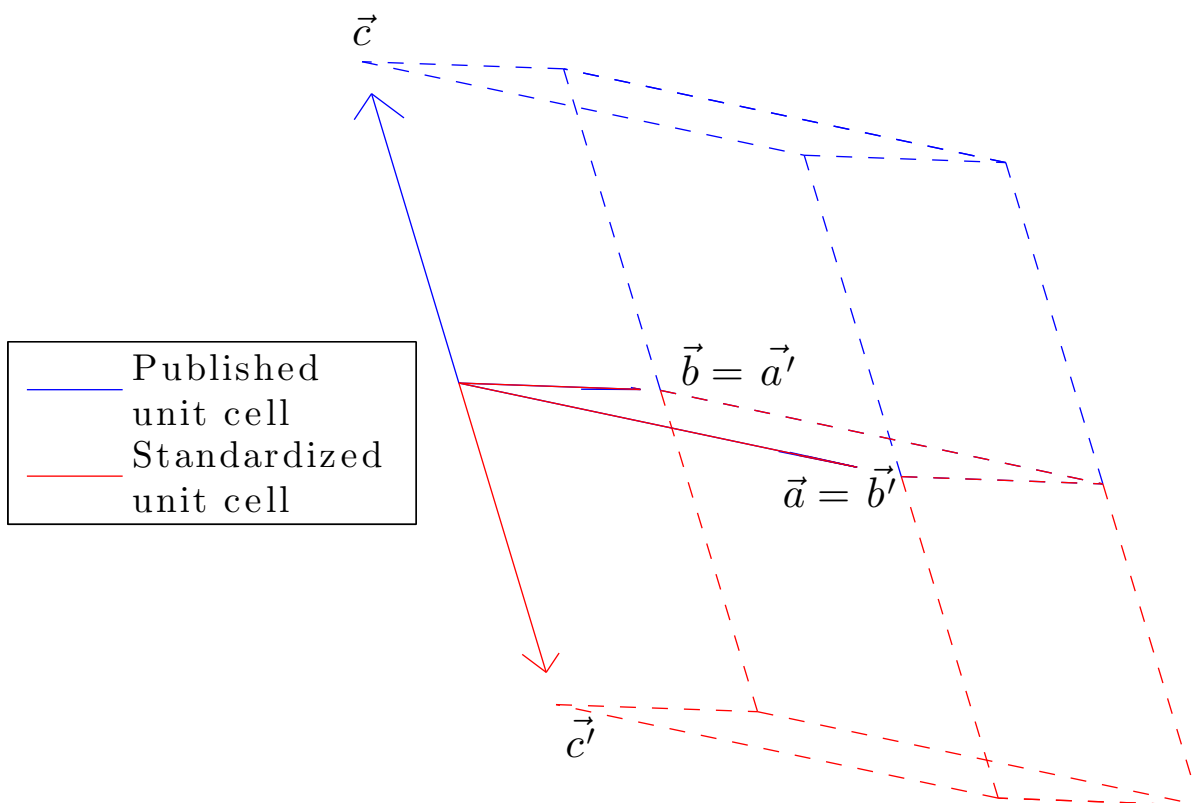
Figure A.1: Standardized malonic acid unit cell as published in 1957 [24]. The published unit cell vectors are in blue while the standardized ones are in red. We can see that the standardization does not change the representation of the crystalline structure.

Appendix B

Mathematical notations

B.1 Pauli matrices

The Pauli matrices along with the identity matrix form a basis of the 2×2 matrices.

$$\mathbb{1} = \begin{bmatrix} 1 & 0 \\ 0 & 1 \end{bmatrix} \quad X = \begin{bmatrix} 0 & 1 \\ 1 & 0 \end{bmatrix} \quad Y = \begin{bmatrix} 0 & -i \\ i & 0 \end{bmatrix} \quad Z = \begin{bmatrix} 1 & 0 \\ 0 & -1 \end{bmatrix}$$

B.2 Spin operators

$$\hat{S}_Z = Z \otimes \underbrace{\mathbb{1} \otimes \mathbb{1} \otimes \cdots \otimes \mathbb{1}}_{\text{number of nuclear spins}} \quad \text{as the first spin is the electron spin.}$$

$$\hat{I}_{n,X} = \underbrace{\mathbb{1} \otimes \mathbb{1} \otimes \mathbb{1} \otimes \cdots \otimes \underbrace{X}_{(n+1)^{\text{th}} \text{ position}} \otimes \cdots \otimes \mathbb{1}}_{\text{number of nuclear spins}}$$

$$\hat{I}_{n,Z} = \underbrace{\mathbb{1} \otimes \mathbb{1} \otimes \mathbb{1} \otimes \cdots \otimes \underbrace{Z}_{(n+1)^{\text{th}} \text{ position}} \otimes \cdots \otimes \mathbb{1}}_{\text{number of nuclear spins}}$$

Appendix C

Magnetic field orientation and Hamiltonian using spherical coordinates

For some of the simulation and optimization programs, we made the choice to work with an axis system where the external magnetic field $\vec{B}$ is aligned with the x-axis. To model the rotation of the sample with respect to the magnetic field (which has a constant direction in the laboratory frame), to simulate CW experiments for instance, we only need to describe the change of orientation of the field with respect to the previous axes definition.

This means that we can temporarily work with the normalized external magnetic field $\bar{B}$. Since it is a normalized vector, its direction can be described as the direction between the centre of the axis system O and a sphere of radius 1 centred on O. We will naturally call this new direction x_R. In spherical coordinates, since x_R is unitary, we then only need two coordinates to fully characterize x_R: θ and φ.

When it comes to getting the Hamiltonian of a sample we know in a new frame, not only do we need to know the direction of x_R, but we also have to know precisely the directions of y_R and z_R. Indeed, as explained in section 3.1.1, when the magnetic field is pointing in

the $\vec{x}$ direction, the Hamiltonian of the sample can be written as:

$$\hat{H} = \omega_S \hat{S}_Z + \sum_{n=1}^{K} \omega_n \hat{I}_{n,Z} + \sum_{n=1}^{K} a_n \hat{S}_Z \hat{I}_{n,Z} + \sum_{n=1}^{K} b_n \hat{S}_Z \hat{I}_{n,X} \tag{C.1}$$

$$\text{Where}: a_n = \vec{A}_{n,xx} \text{ and } b_n = \sqrt{\vec{A}_{n,xy}^2 + \vec{A}_{n,xz}^2}$$

$$\omega_S = \frac{g_{xx}\mu_B}{h}\|\vec{B}_0\|$$

As a consequence, we have to introduce the most natural rotation to go from our initial axis system (x, y, z) to (x_R, y_R, z_R). In spherical coordinates, this rotation can be decomposed into two rotations: one rotation of φ around z turns (x, y, z) into $(x\prime, y\prime, z\prime)$, while a second rotation of $\frac{\pi}{2} - \theta$ around $y\prime$ turns $(x\prime, y\prime, z\prime)$ into (x_R, y_R, z_R). The overall rotation will be denoted $R(\theta, \varphi)$.

As for the expression of the new Hamiltonian, it can be obtained by expressing the tensors in the new frame. The $\vec{g}$-tensor as well as the hyperfine tensors have to be expressed in this new frame in order to obtain the correct Hamiltonian. We have to be careful though: when the sample is rotated in a certain direction with respect to the magnet, the magnetic field is rotated in the opposite direction with respect to the crystal.

$$\vec{\Gamma}_R = R(\theta, \varphi)^\dagger \cdot \vec{\Gamma} \cdot R(\theta, \varphi) \tag{C.2}$$

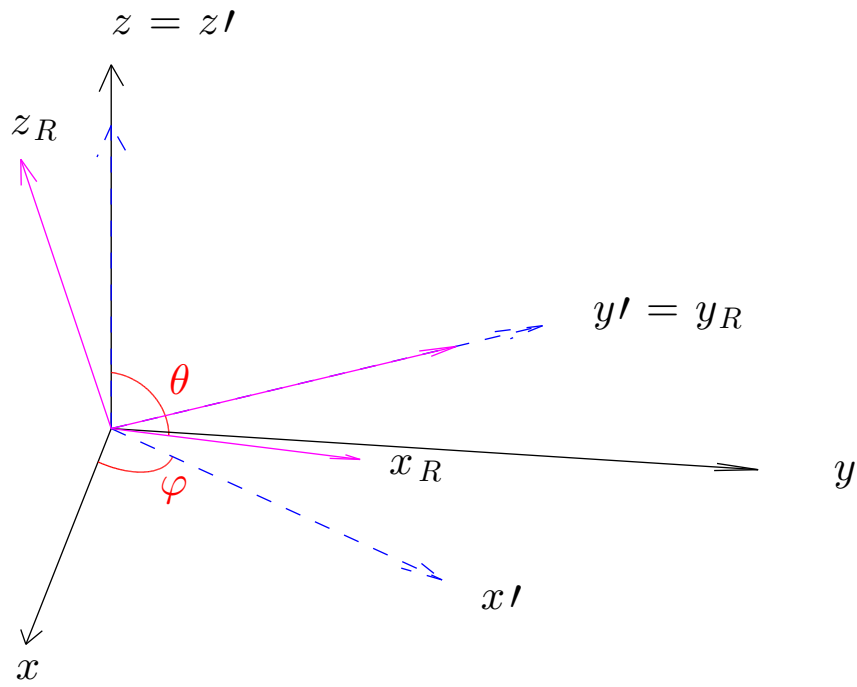Figure C.1: Rotation to describe the new orientation of the magnetic field in spherical coordinates. The initial frame is (x, y, z) (black solid arrows). A rotation of φ around z turns (x, y, z) into $(x\prime, y\prime, z\prime)$ (blue dashed arrows). A second rotation of $\frac{\pi}{2} - \theta$ around $y\prime$ turns $(x\prime, y\prime, z\prime)$ into (x_R, y_R, z_R) (magenta solid arrows).

Appendix D

Miller indices and surface indexing analysis

A surface can easily be defined as an ensemble of vectors orthogonal to the *normal vector* of the surface. Surfaces on a crystal can be characterized by their Miller index. The Miller index $[x, y, z]$ of a surface S, given the crystal's unit cell vectors $(\vec{a}, \vec{b}, \vec{c})$, denotes the surface containing the points $x\vec{a}$, $y\vec{b}$ and $z\vec{c}$, unless some of x, y or z is 0. In that case, the surface is parallel to every axis related to a 0 index.

In this situation, relating a Miller index to a normal vector of a surface depends on the structure of the crystal. For crystals which structure consists of 3 orthogonal vectors, the Miller index actually directly provides the coordinates of the normal vector of the surface in the $(\vec{a}, \vec{b}, \vec{c})$ axis system. For other structures, like the triclinic crystal structure, things are slightly more complex, due to the non-orthogonality between $\vec{a}$, $\vec{b}$ and $\vec{c}$.

We then have to go back to the original definition and, provided we have the direction cosines of $\vec{a}$, $\vec{b}$ and $\vec{c}$ in an orthonormal axis system, we can work out a value for the normal vector of the surface. To do this, we first chose the 3 points needed to unambiguously define the surface. If the considered Miller index does not contain any 0, the three points are $x\vec{a}$, $y\vec{b}$ and $z\vec{c}$. If the Miller index contains one or more zeros, say $x \neq 0$, we still know at least one point (here $M_1 = x\vec{a} \in S$). We then know that the surface is parallel to the axes related to a 0 index: if $y = 0$, $M_1 + \vec{b} \in S$, and similarly, if $z = 0$, $M_1 + \vec{c} \in S$.

Given these three points M_1, M_2, M_3, belonging to the surface, it is easy to find the normal vector of the surface.

$$\{M_1, M_2, M_3\} \in S \Rightarrow M_1\vec{M_2}, M_2\vec{M_3} \in S$$
$$\Rightarrow \vec{n} = M_1\vec{M_2} \times M_2\vec{M_3} \perp S$$

To complete this surface characterization, we can first normalize $\vec{n}$ and secondly make sure that it is an outer-pointing normal. That means checking $\vec{n} \cdot O\vec{M_j} > 0$ for $j = 1, 2$ or 3.
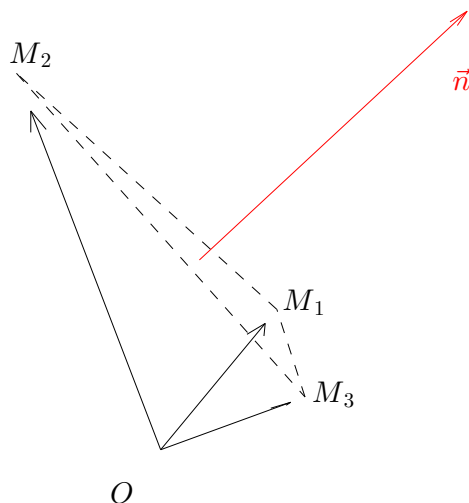

Figure D.1: Normal to a surface defined by 3 points. The 3 points M_1, M_2 and M_3 (solid black) form the surface S (dashed black) and allow us to 4 calculate the direction cosines of the normal vector $\vec{n}$ (solid red). It is clear from the $O\vec{M_j}$ ($j = 1, 2$ or 3) that $\vec{n}$ is an outer-pointing normal vector.
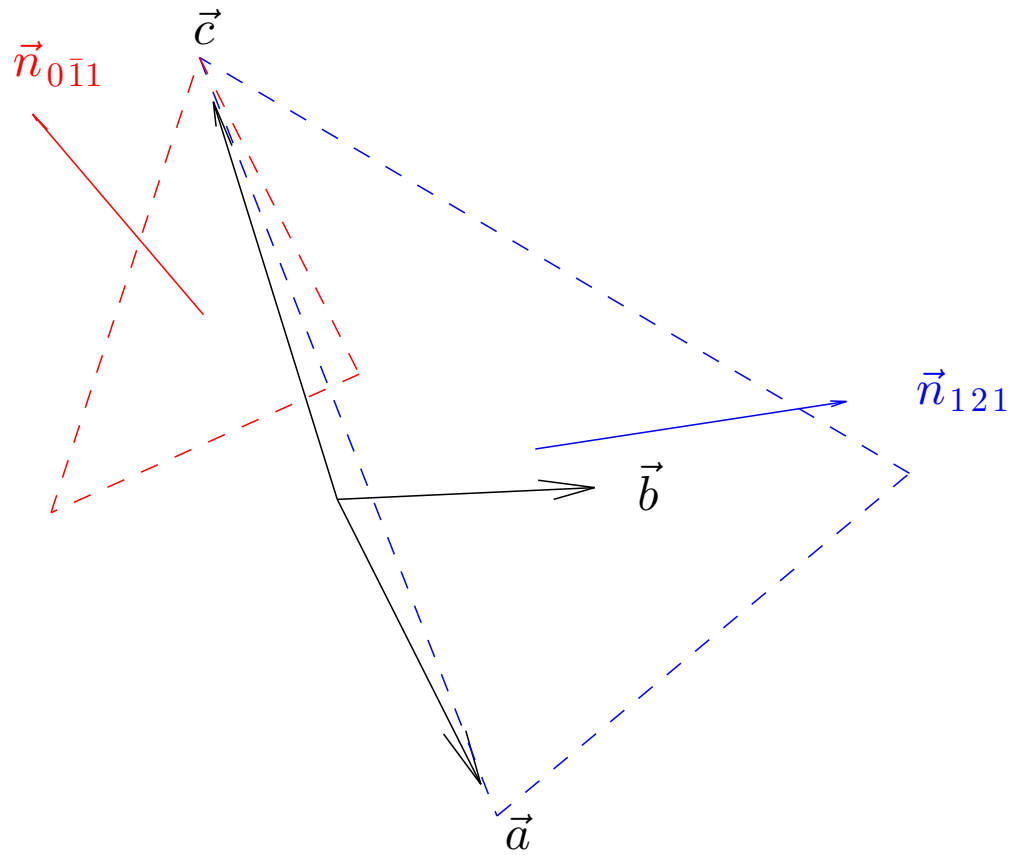
Figure D.2: Surfaces designated by Miller indices for a triclinic crystal. The 3 vectors of the unit cell are $\vec{a}$, $\vec{b}$ and $\vec{c}$. The red surface is denoted by the Miller index $0\bar{1}1$ and hence parallel to $\vec{a}$. The blue surface corresponds to 121 in terms of Miller index.

References

[1] Alan Mathison Turing. On computable numbers, with an application to the entschei-dungsproblem. *J. of Math*, 58:345–363, 1936.

[2] John Bardeen and Walter Hauser Brattain. The transistor, a semi-conductor triode. *Physical Review*, 74(2):230, 1948.

[3] Richard P Feynman. Quantum mechanical computers. *Foundations of physics*, 16(6):507–531, 1986.

[4] Lov K Grover. A fast quantum mechanical algorithm for database search. In *Proceedings of the twenty-eighth annual ACM symposium on Theory of computing*, pages 212–219. ACM, 1996.

[5] Peter W Shor. Algorithms for quantum computation: discrete logarithms and factoring. In *Foundations of Computer Science, 1994 Proceedings., 35th Annual Symposium on*, pages 124–134. IEEE, 1994.

[6] Ronald L Rivest, Adi Shamir, and Len Adleman. A method for obtaining digital signatures and public-key cryptosystems. *Communications of the ACM*, 21(2):120–126, 1978.

[7] D. P. DiVincenzo. The physical implementation of quantum computation. *Fortsch. Phys.*, 48:771–793, 2000.

[8] Juan I Cirac and Peter Zoller. Quantum computations with cold trapped ions. *Physical review letters*, 74(20):4091, 1995.

[9] Thomas Monz, Philipp Schindler, Julio T Barreiro, Michael Chwalla, Daniel Nigg, William A Coish, Maximilian Harlander, Wolfgang Hänsel, Markus Hennrich, and Rainer Blatt. 14-qubit entanglement: Creation and coherence. *Physical Review Letters*, 106(13):130506, 2011.

[10] Emanuel Knill and Raymond Laflamme. Theory of quantum error-correcting codes. *Physical Review A*, 55(2):900, 1997.

[11] David G Cory, MD Price, W Maas, E Knill, Raymond Laflamme, Wojciech H Zurek, Timothy F Havel, and SS Somaroo. Experimental quantum error correction. *Physical Review Letters*, 81(10):2152, 1998.

[12] E Knill, R Laflamme, R Martinez, and C Negrevergne. Benchmarking quantum computers: The five-qubit error correcting code. *Physical Review Letters*, 86(25):5811, 2001.

[13] Nicolas Boulant, Lorenza Viola, Evan M Fortunato, and David G Cory. Experimental implementation of a concatenated quantum error-correcting code. *Physical review letters*, 94(13):130501, 2005.

[14] Osama Moussa, Jonathan Baugh, Colm A Ryan, and Raymond Laflamme. Demonstration of sufficient control for two rounds of quantum error correction in a solid state ensemble quantum information processor. *Physical review letters*, 107(16):160501, 2011.

[15] J Chiaverini, D Leibfried, T Schaetz, MD Barrett, RB Blakestad, J Britton, WM Itano, JD Jost, E Knill, C Langer, et al. Realization of quantum error correction. *Nature*, 432(7017):602–605, 2004.

[16] Philipp Schindler, Julio T Barreiro, Thomas Monz, Volckmar Nebendahl, Daniel Nigg, Michael Chwalla, Markus Hennrich, and Rainer Blatt. Experimental repetitive quantum error correction. *Science*, 332(6033):1059–1061, 2011.

[17] MD Reed, L DiCarlo, SE Nigg, L Sun, L Frunzio, SM Girvin, and RJ Schoelkopf. Realization of three-qubit quantum error correction with superconducting circuits. *Nature*, 482(7385):382–385, 2012.

[18] G Waldherr, Y Wang, S Zaiser, M Jamali, T Schulte-Herbrüggen, H Abe, T Ohshima, J Isoya, JF Du, P Neumann, et al. Quantum error correction in a solid-state hybrid spin register. *Nature*, 2014.

[19] T Cole, C Heller, and HM McConnell. Electron magnetic resonance of CH(COOH)2. *Proceedings of the National Academy of Sciences of the United States of America*, 45(4):525, 1959.

[20] HM McConnell, C Heller, T Cole, and RW Fessenden. Radiation damage in organic crystals. I. CH (COOH) 2 in Malonic Acid. *Journal of the American Chemical Society*, 82(4):766–775, 1960.

[21] A Horsfield, JR Morton, and DH Whiffen. Electron spin resonance of γ-irradiated malonic acid. *Molecular Physics*, 4(4):327–332, 1961.

[22] M Mehring, J Mende, and W Scherer. Entanglement between an electron and a nuclear spin 1 2. *Physical review letters*, 90(15):153001, 2003.

[23] A Gerstäcker, H. Möller, and A. Reis. *Zeitschrift für Kristallographie*, 66:421, 1928.

[24] J. A. Goedkoop and C. H. MacGillavry. The crystal structure of malonic acid. *Acta Crystallographica*, 10(2):125–127, Feb 1957.

[25] NR Jagannathan, SS Rajan, and E Subramanian. Refinement of the crystal structure of malonic acid, C3H4O4. *Journal of chemical crystallography*, 24(1):75–78, 1994.

[26] NM Atherton. *Principles of electron spin resonance*. Ellis Horwood Limited, 1993.

[27] Michael A Christie, James Glimm, John W Grove, David M Higdon, David H Sharp, and Merri M Wood-Schultz. Error analysis and simulations of complex phenomena. *Los Alamos Science*, 29(6), 2005.

[28] Martin Basil, C Papadopoulos, D Sutherland, and H Yeung. Application of probabilistic uncertainty methods (monte carlo simulation) in flow measurement uncertainty estimation. In *Flow Measurement 2001-International Conference*, pages S178–188, 2001.

[29] Junseog Kang, Sibel Tokdemir, Jun Shao, and William H Nelson. Electronic g-factor measurement from ENDOR-induced EPR patterns: malonic acid and guanine hydrochloride dihydrate. *Journal of Magnetic Resonance*, 165(1):128–136, 2003.

[30] T Cole and C Heller. Hyperfine splittings in the (HOOC) $C^{13}H$ (COOH) radical. *Journal of Chemical Physics*, 34:1085–1086, 1961.

[31] Arthur Schweiger and Gunnar Jeschke. *Principles of pulse electron paramagnetic resonance*. Oxford University Press, 2001.

[32] Martin Laforest. *Error characterization and quantum control benchmarking in liquid state NMR using quantum information processing techniques*. PhD thesis, University of Waterloo, 2008.

[33] Jeremy Chamilliard. On an electron spin resonance spectrometer for quantum information processing. Master's thesis, University of Waterloo, 2011.

[34] Yingjie Zhang. Universal control in 1e-2n spin system utilizing anisotropic hyperfine interactions. Master's thesis, University of Waterloo, 2010.

[35] George A Rinard, Richard W Quine, Sandra S Eaton, and Gareth R Eaton. Microwave coupling structures for spectroscopy. *Journal of Magnetic Resonance, Series A*, 105(2):137–144, 1993.

[36] Ragnar Bergene and Thor B Melø. Free radicals in malonic acid: A study of radical conformations at 77 K and 295 K by the ESR-technique. *Biophysik*, 9(1):1–12, 1972.

[37] J Baugh, J Chamilliard, CM Chandrashekar, M Ditty, A Hubbard, R Laflamme, M Laforest, D Maslov, O Moussa, C Negrevergne, et al. Quantum information processing using nuclear and electron magnetic resonance: review and prospects. *arXiv preprint arXiv:0710.1447*, 2007.

[38] Yingjie Zhang, Colm A Ryan, Raymond Laflamme, and Jonathan Baugh. Coherent control of two nuclear spins using the anisotropic hyperfine interaction. *Physical review letters*, 107(17):170503, 2011.

[39] Navin Khaneja, Timo Reiss, Cindie Kehlet, Thomas Schulte-Herbrüggen, and Steffen J Glaser. Optimal control of coupled spin dynamics: design of NMR pulse sequences by gradient ascent algorithms. *Journal of Magnetic Resonance*, 172(2):296–305, 2005.

[40] E. Knill, D. Leibfried, R. Reichle, J. Britton, R. B. Blakestad, J. D. Jost, C. Langer, R. Ozeri, S. Seidelin, and D. J. Wineland. Randomized benchmarking of quantum gates. *Phys. Rev. A*, 77:012307, Jan 2008.

[41] Gilles Brassard, Yuval Elias, Tal Mor, and Yossi Weinstein. Prospects and limitations of algorithmic cooling. *arXiv preprint arXiv:1404.6824*, 2014.

[42] Osama Moussa. On heat-bath algorithmic cooling and its implementation in solid-state NMR. Master's thesis, University of Waterloo, 2005.

[43] Jonathan Baugh, Osama Moussa, Colm A Ryan, Ashwin Nayak, and Raymond Laflamme. Experimental implementation of heat-bath algorithmic cooling using solid-state nuclear magnetic resonance. *Nature*, 438(7067):470–473, 2005.

[44] Ben Criger, Osama Moussa, and Raymond Laflamme. Quantum error correction with mixed ancilla qubits. *Physical Review A*, 85(4):044302, 2012.